


Constraining parameters of low mass merging compact binary systems with Einstein Telescope alone

Neha Singh^{*}

*Laboratoire d'Annecy-le-Vieux de Physique Théorique (LAPTh), USMB, CNRS, F-74940 Annecy, France
Astronomical Observatory, University of Warsaw, Aleje Ujazdowskie 4, 00-478 Warsaw, Poland*

Tomasz Bulik[†]

Astronomical Observatory, University of Warsaw, Aleje Ujazdowskie 4, 00-478 Warsaw, Poland

 (Received 23 July 2021; revised 25 November 2021; accepted 28 November 2022; published 15 December 2022)

The Einstein Telescope (ET), a future third-generation gravitational wave detector, will have detection sensitivity for gravitational wave signals down to 1 Hz. This improved low-frequency sensitivity of the ET will allow the observation of low mass binaries for a longer period of time in the detection band before their merger. Because of an improved sensitivity as compared to current and advanced 2G detectors, the detection rate will also be greatly improved. Given the high detection rate of merging compact binaries with the ET, it will be a useful instrument to conduct population studies. In this paper, we present an algorithm to estimate the parameters of the low mass merging compact binary systems such as localization, chirp mass, redshift, mass ratios, and total mass of the source, which are crucial in order to estimate the capability of the ET to study various compact binary populations. For the compact binary population distributed uniformly in comoving volume, we find that with single ET, $\approx 1\%$ of binaries can be localized within 800 square degrees. The values of chirp mass and total mass can be constrained within $\lesssim 5\%$ error, while z and D_L can be estimated with an error of $\lesssim 15\%$ for effective SNR $\gtrsim 50$ using single ET.

DOI: [10.1103/PhysRevD.106.123014](https://doi.org/10.1103/PhysRevD.106.123014)

I. INTRODUCTION

The second-generation gravitational wave (GW) detectors initiated GW astronomy with the first detection of merging compact objects GW150914 [1], which was the direct detection of a binary black hole (BBH). Numerous BBH detections in the next run since then have shown the existence of a population of stellar-mass black holes (BHs) undetected in previous observations which is much heavier than those detected through the observation of x-ray binaries [2–5]. The first detection of a binary neutron star (BNS) inspiral [6] with simultaneous gamma-ray burst observation and the subsequent detection of the electromagnetic counterpart provided a better understanding of the origin of short gamma-ray bursts [7–13]. The observations of the associated kilonova proved that the BNS mergers source the formation of the heaviest metals through r-process nucleosynthesis. The joint detection of GW and gamma-ray bursts proved the speed of GWs and the speed of light to be equal with an accuracy of 1 in 10^{15} [9].

Detailed studies of GW sources in the Universe will be continued with 3G detectors such as ET [14,15] or Cosmic

Explorer (CE) [16–18]. ET is planned to have a detection sensitivity down to 1 Hz [19,20]. This is required so as to have the ability to detect BBHs with components of higher mass such as 10^2 – $10^4 M_\odot$ [21–24] which are yet to be detected.

Given the improvement in sensitivity by a factor of 10 in the intermediate frequency range, and several orders of magnitude improvement in the low-frequency band, as compared to 2G detectors, ET will be able to detect systems such as BBH and neutron star–black hole (NSBH) binaries of total mass in the range of 20– $100 M_\odot$, up to redshift $z \sim 20$; high mass BHs with masses of the order $10^3 M_\odot$ up to $z \sim (1-5)$; BNS binaries of total masses $\sim 3 M_\odot$ up to $z \sim (2-3)$ [25,26]. The detection rate will also be greatly improved as compared to the current and advanced 2G detectors. The expected detection rates based on the ET-D [14] design sensitivity are $\sim 10^5$ – 10^6 BBH detections and $\sim 7 \times 10^4$ BNS detections in one year [27–29].

Because of an improved low-frequency sensitivity, ET will observe low mass binaries for a longer period of time in the detection band before their merger. With the lowest frequency detection sensitivity for ET-D being down to 1 Hz, the BNS signals can stay in the detectable band from a few minutes to several days. Thus, it is necessary to take into account the effect of rotation of Earth on the response function. Zhao and Wen [30] and Chan *et al.* [31] have

^{*}singh@lapth.cnrs.fr

[†]tb@astrouw.edu.pl

done such an analysis using a Fisher information matrix to study the effects of the time-dependent detector response due to Earth's rotation on long-duration signals from systems such as BNS and NSBH for estimating the uncertainties in the measurement of signal parameters using 3G detectors such as ET and CE. In the previous work [32], we presented an algorithm to localize and constrain the parameters of BBH coalescences such as the chirp mass \mathcal{M} and redshift z or luminosity distance D_L using single ET. In this work, we continue to explore the capability of ET as a single instrument to study longer-duration signals from coalescing low mass compact binary systems and present a simplified approach to estimate the parameters of low mass merging compact binary systems. Given the high detection rate of merging compact binaries with ET, it will be a useful instrument for conducting population studies. We present an algorithm to estimate the angles describing the location of the source, the inclination, and polarization of an inspiralling compact binary system using the ratios of the signal to noise ratios (SNRs) generated in each of the three detectors in single ET. We also demonstrate that single ET can break the chirp mass–redshift degeneracy and, thus, provide estimates of the chirp mass, redshift, mass ratios, and total mass of the source. These estimates are crucial in order to estimate the capability of ET to study various compact binary populations [33].

II. ET AS A SINGLE INSTRUMENT

The ET will comprise of three coplanar detectors of equal arm length of 10 km, aligned in the form of an equilateral triangle so that the opening angle will be 60° and it will use Michelson interferometry. Multiple design configurations have been studied over time. The first basic design considered was ET-B [19]. It was based on a single cryogenic interferometer and covered the full frequency range of interest. It was then updated to a xylophone design, resulting in the ET-C sensitivity [20] in which each detector consisted of two interferometers, each with an opening angle of 60° , with one optimized for low frequencies and the other optimized for high frequencies. ET-D [14] is a realistic version of ET-C, since it considers an improved noise model. Each ET detector will have two interferometers, one each for the low and high frequencies. The final triangular design of the ET will have three such detectors and so six interferometers in total.

While observing a GW signal which stays in the detection band of the detector for a long duration, one has to take into account the change in the antenna response with the rotation of Earth. Following the detailed treatment given in Jaranowski, Królak, and Schutz [34], which takes into account the motion of Earth, the time-dependent antenna response function for a single detector in the reference frame of the celestial sphere at time t is given as

$$F_+(t) = \sin \eta [a(t) \cos 2\psi + b(t) \sin 2\psi], \quad (1a)$$

$$F_\times(t) = \sin \eta [b(t) \cos 2\psi - a(t) \sin 2\psi], \quad (1b)$$

where

$$\begin{aligned} a(t) = & \frac{1}{16} \sin 2\gamma (3 - \cos 2\lambda)(3 - \cos 2\delta) \\ & \times \cos[2(\alpha - \phi_r - \Omega_r t)] \\ & - \frac{1}{4} \cos 2\gamma \sin \lambda (3 - \cos 2\delta) \sin[2(\alpha - \phi_r - \Omega_r t)] \\ & + \frac{1}{4} \sin 2\gamma \sin 2\lambda \sin 2\delta \cos[\alpha - \phi_r - \Omega_r t] \\ & - \frac{1}{2} \cos 2\gamma \cos \lambda \sin 2\delta \sin[\alpha - \phi_r - \Omega_r t] \\ & + \frac{3}{4} \sin 2\gamma \cos^2 \lambda \cos^2 \delta \end{aligned} \quad (2a)$$

and

$$\begin{aligned} b(t) = & \cos 2\gamma \sin \lambda \sin \delta \cos[2(\alpha - \phi_r - \Omega_r t)] \\ & + \frac{1}{4} \sin 2\gamma (3 - \cos 2\lambda) \sin \delta \sin[2(\alpha - \phi_r - \Omega_r t)] \\ & + \cos 2\gamma \cos \lambda \cos \delta \cos[\alpha - \phi_r - \Omega_r t] \\ & + \frac{1}{2} \sin 2\gamma \sin 2\lambda \cos \delta \sin[\alpha - \phi_r - \Omega_r t], \end{aligned} \quad (2b)$$

where α is the right ascension, δ is the declination of the GW source, ψ is the polarization angle, and λ is the latitude for the detector location. Ω_r is Earth's rotational angular velocity, and ϕ_r is the phase defining the position of Earth in its diurnal motion at $t = 0$. The quantity $(\phi_r + \Omega_r t)$ is the local sidereal time at the detector site, measured in radians, while γ determines the orientation of the detector arms and is measured counterclockwise from East to the bisector of the interferometer arms. Finally, η is the angle between the interferometer arms. In the case of ET, $\eta = 60^\circ$.

Using Eq. (1), the antenna response functions can be calculated for any given instant of time t . We use the currently planned design of ET-D [14], consisting of three overlapping detectors, arranged in an equilateral configuration with arm-opening angles of 60° . The location of ET detector for our analysis is chosen to be at the Virgo site [35,36].

III. SIGNAL CHARACTERISTICS OF COALESCING COMPACT BINARY SYSTEMS

We consider ET as a single instrument rather than a part of network to detect the gravitational radiation from an inspiralling compact binary system in this work. Inspiralling compact binary systems are also known as chirping binaries. The two polarizations of the GW signal

from such a system have a monotonically increasing frequency and amplitude with the orbital motion radiating away GW energy. If t_c is the time of the termination of the waveform, then the two polarizations h_+ and h_\times , of the waveform at time $t < t_c$ for a binary with the chirp mass \mathcal{M} , merging at a distance D_L (described in Sec. III in Ref. [37]) are given as

$$h_+(t) = -\frac{1 + \cos^2 \iota}{2} \left(\frac{G\mathcal{M}}{c^2 D_L} \right) \left(\frac{t_c - t}{5G\mathcal{M}/c^3} \right)^{-1/4} \times \cos [2\Phi_c + 2\Phi(t - t_c; M, \mu)], \quad (3a)$$

$$h_\times(t) = -\cos \iota \left(\frac{G\mathcal{M}}{c^2 D_L} \right) \left(\frac{t_c - t}{5G\mathcal{M}/c^3} \right)^{-1/4} \times \sin [2\Phi_c + 2\Phi(t - t_c; M, \mu)], \quad (3b)$$

where c is the speed of light, G is the gravitational constant, and ι is the angle of inclination of the orbital plane of the binary system with respect to the observer. μ is the reduced mass of the binary system. The angle $\Phi(t - t_c; M, \mu)$ gives the orbital phase of the binary system. The chirp mass \mathcal{M} for a binary system composed of component masses m_1 and m_2 is defined as $\mathcal{M} = (m_1 m_2)^{3/5} / M^{1/5}$, where $M = m_1 + m_2$ is the total mass and Φ_c is the phase of the termination of the waveform [37]. The strain in the detector is given as

$$h(t) = F_+(t)h_+(t + t_c - t_0) + F_\times(t)h_\times(t + t_c - t_0), \quad (4)$$

where F_+ and F_\times are the antenna response function of one of the three detectors in ET, as defined in Eq. (1), t_0 is the time of coalescence in the detector frame, and $(t_0 - t_c)$ is the travel of time from the source to the detector. Substituting the values of the two polarizations from Eq. (3) in Eq. (4) gives the value of strain

$$h(t) = -\left(\frac{G\mathcal{M}}{c^2} \right) \left(\frac{\Theta}{4D_L} \right) \left(\frac{t_0 - t}{5G\mathcal{M}/c^3} \right)^{-1/4} \times \cos [2\Phi_0 + 2\Phi(t - t_c; M, \mu)], \quad (5)$$

where

$$\Theta \equiv 2[F_+^2(1 + \cos^2 \iota)^2 + 4F_\times^2 \cos^2 \iota]^{1/2} \quad (6)$$

and

$$2\Phi_0 = 2\Phi_c - \arctan \left(\frac{2F_\times \cos \iota}{F_+(1 + \cos^2 \iota)} \right) \quad (7)$$

with $0 < \Theta < 4$.

In a given duration, for which it can be assumed that the time of the signal in the detector bandwidth is short enough to ignore the change in the antenna response functions of the detector due to rotation of Earth, the Fourier transform of the GW signal amplitude $h(t)$ in terms of frequency f is [38–40]

$$|\tilde{h}(f)| = \frac{2c}{D_L} \left(\frac{5G\mu}{96c^3} \right)^{1/2} \left(\frac{G\mathcal{M}}{\pi^2 c^3} \right)^{1/3} \left(\frac{\Theta}{4} \right) f^{-7/6}. \quad (8)$$

The SNR ρ_j for $j = (1, 2, 3)$ for each of the three ET detectors, obtained using match-filtering assuming that they have identical noise, is given as [39,41]

$$\rho_j \approx 8\Theta_j \frac{r_0}{D_L} \left(\frac{\mathcal{M}_z}{\mathcal{M}_{BNS}} \right)^{5/6} \sqrt{\zeta(f_{\max})}, \quad (9)$$

where $\mathcal{M}_z = (1 + z)\mathcal{M}$ is the redshifted chirp mass. $\mathcal{M}_{BNS} \approx 1.218M_\odot$ is the chirp mass of an equal mass binary with each component mass being $1.4M_\odot$, while

$$\zeta(f_{\max}) = \frac{1}{x_{7/3}} \int_1^{2f_{\max}} \frac{df(\pi M_\odot)^2}{(\pi f M_\odot)^{7/3} S_h(f)}, \quad (10)$$

where $S_h(f)$ is the power spectral density (PSD) for ET-D configuration for the ET-D noise curve [14] and

$$x_{7/3} = \int_{1 \text{ Hz}}^\infty \frac{df(\pi M_\odot)^2}{(\pi f M_\odot)^{7/3} S_h(f)}. \quad (11)$$

The characteristic distance sensitivity r_0 is

$$r_0^2 = \frac{5}{192\pi} \left(\frac{3G}{20} \right)^{5/3} x_{7/3} \frac{M_\odot^2}{c^3}. \quad (12)$$

The frequency at the end of the inspiral phase f_{\max} is given as

$$f_{\max} = 785 \left(\frac{M_{BNS}}{M(1+z)} \right) \text{ Hz}, \quad (13)$$

where $M_{BNS} = 2.8M_\odot$ is the total mass of an equal mass binary with each component mass of $1.4M_\odot$. We can define the combined effective SNR for the combined signal from three detectors as

$$\rho_{\text{eff}} = 8\Theta_{\text{eff}} \frac{r_0}{D_L} \left(\frac{\mathcal{M}_z}{1.2M_\odot} \right)^{5/6} \sqrt{\zeta(f_{\max})}, \quad (14)$$

where the effective antenna response function Θ_{eff} is

$$\Theta_{\text{eff}} = (\Theta_1^2 + \Theta_2^2 + \Theta_3^2)^{1/2}. \quad (15)$$

IV. THE PLAN OF THE ANALYSIS

We use the response functions given by Eq. (1), as defined in Sec. II, in the celestial sphere frame of Ref. [34], for this long-duration signal analysis. Assuming that the response functions do not change much during 5 min, we divide the inspiral signal into 5-min segments from the time it enters the detection band at 1 Hz. The duration of the last

segment will be ≤ 5 min, since it is limited by f_{\max} , the frequency at the end of the inspiral, given by Eq. (13).

We assume that, in the case of detection of a coalescing low mass binary system, the observables D are as follows: (a) The three SNRs ρ_j^i defined by Eq. (9) for each i th segment of the signal. (b) The phase of the strain $\Phi_{o,j}^i$ for $j = (1, 2, 3)$ corresponding to three detectors, defined in Eq. (7) for each i th segment of the signal. The quantity Φ_0 is the best match phase obtained by maximizing the matched-filter output over the phase of the strain $h(t)$. The details are given in Ref. [37]. (c) The GW frequency at the start and end of each segment of the detected signal. (d) The redshifted chirp mass \mathcal{M}_z . (e) The frequency at the end of the inspiral, corresponding to the innermost stable circular orbit, f_{\max} .

The observed GW frequency f_{gw}^{obs} can be calculated using Eq. (4.195) in Maggiore [42]:

$$f_{gw}^{\text{obs}} = \frac{1}{\pi} \left(\frac{5}{256} \frac{1}{\tau_{\text{obs}}} \right)^{3/8} \left(\frac{G\mathcal{M}_z}{c^3} \right)^{-5/8}, \quad (16)$$

where τ_{obs} is the time to coalescence measured in the observer's frame. The minimum frequency for the detection sensitivity of the detector and the frequency f_{\max} sets the limit on τ_{obs} spent in the detection band.

If τ_{i-1} and τ_i are the start and end values of τ_{obs} , respectively, for the i th segment, then the corresponding values f_{i-1} and f_i of f_{gw}^{obs} will be

$$f_{i-1} = \frac{1}{\pi} \left(\frac{5}{256} \frac{1}{\tau_{i-1}} \right)^{3/8} \left(\frac{G\mathcal{M}_z}{c^3} \right)^{-5/8} \quad (17)$$

and

$$f_i = \frac{1}{\pi} \left(\frac{5}{256} \frac{1}{\tau_i} \right)^{3/8} \left(\frac{G\mathcal{M}_z}{c^3} \right)^{-5/8}. \quad (18)$$

In order to constrain the angles defining the strain in the detector, we use the ratios of SNR in each segment. The SNR for the i th segment in the j th detector can be written using Eq. (9) as

$$\rho_j^i \approx 8\Theta_j^i \frac{r_0}{D_L} \left(\frac{\mathcal{M}_z}{\mathcal{M}_{BNS}} \right)^{5/6} \sqrt{\zeta^i(f_{i-1}, f_i)}, \quad (19)$$

where

$$\zeta^i(f_{i-1}, f_i) = \frac{1}{x_{7/3}} \int_{f_{i-1}}^{f_i} \frac{df (\pi M_\odot)^2}{(\pi f M_\odot)^{7/3} S_h(f)} \quad (20)$$

and

$$\Theta_j^i \equiv 2[(F_+^i)^2(1 + \cos^2 \iota)^2 + 4(F_\times^i)^2 \cos^2 \iota]_j^{1/2}, \quad (21)$$

where F_+^i and F_\times^i are the antenna response functions for the j th detector in the i th segment. The effective SNR for the i th segment is

$$\rho_{\text{eff}}^i = 8\Theta_{\text{eff}}^i \frac{r_0}{D_L} \left(\frac{\mathcal{M}_z}{1.2M_\odot} \right)^{5/6} \sqrt{\zeta^i(f_{i-1}, f_i)}, \quad (22)$$

where

$$(\rho_{\text{eff}}^i)^2 = (\rho_1^i)^2 + (\rho_2^i)^2 + (\rho_3^i)^2 \quad (23)$$

and the function Θ_{eff}^i is

$$(\Theta_{\text{eff}}^i)^2 = (\Theta_1^i)^2 + (\Theta_2^i)^2 + (\Theta_3^i)^2. \quad (24)$$

Using Eq. (7), we can write for the i th segment in the j th detector

$$2\Phi_{0,j}^i = 2\Phi_c - \arctan \left(\frac{2F_{\times j}^i \cos \iota}{F_{+j}^i (1 + \cos^2 \iota)} \right). \quad (25)$$

The antenna response function for the detector is dependent on (δ, α, ψ) as seen from Eq. (1), where δ is the declination, α is the right ascension for the location of the binary on the celestial sphere, and ψ is the polarization angle. Thus, the quantity Θ depends on the four angles $(\delta, \alpha, \iota, \psi)$, as seen from Eq. (6), where ι is the inclination angle of the binary with respect to the direction of observation. We choose $\cos \delta, \alpha/\pi, \cos \iota$, and ψ/π to be uncorrelated and distributed uniformly over the range $[-1, 1]$.

We use the SNRs in each segment for each of the three detectors in the triangular configuration of ET, to constrain the value of the effective antenna pattern. The value of the ratios of the SNRs are denoted as $\rho_{21}^i \equiv \rho_2/\rho_1$, and $\rho_{31}^i \equiv \rho_3/\rho_1$ in the i th segment. We note that, using Eq. (19) for each segment, these ratios are

$$\rho_{21}^i = \frac{\Theta_2^i}{\Theta_1^i} \equiv \Theta_{21}^i \quad \text{and} \quad \rho_{31}^i = \frac{\Theta_3^i}{\Theta_1^i} \equiv \Theta_{31}^i. \quad (26)$$

The difference of the phase Φ_0^i using Eq. (7) for the three detectors in the i th segment is

$$\Phi_{21}^i = \Phi_{0,2}^i - \Phi_{0,1}^i \quad \text{and} \quad \Phi_{31}^i = \Phi_{0,3}^i - \Phi_{0,1}^i. \quad (27)$$

The quantities $\rho_{21}^i, \rho_{31}^i, \Phi_{21}^i$, and Φ_{31}^i depend only on the position on the sky, polarization, and inclination angle of the binary system. Thus, we have constraints on these four angles from Eqs. (26) and (27) for each segment. In this analysis, we assume that the measurement errors on the SNRs is Gaussian with the standard deviations for ρ_j^i and Φ_j^i being $\sigma_\rho = 1$, and $\sigma_\Phi = \pi/\rho$, respectively. Note that this is a conservative assumption in comparison to the errors on

the SNRs of the recent GW detections, mentioned in GWTC-2 [2,43].

The probability densities of the measured SNR ratios $P(\rho_{kj}^i)$ and difference between the orbital phase $P(\Phi_{kj}^i)$ between the k th and j th detectors for the i th segment are

$$P(\rho_{kj}^i) = \int d\rho_k^i d\rho_j^i \delta(\rho_{kj}^i - \rho_k^i/\rho_j^i) P(\rho_k^i) P(\rho_j^i) \quad (28)$$

and

$$P(\Phi_{kj}^i) = \int d\Phi_k^i d\Phi_j^i \delta(\Phi_{kj}^i - (\Phi_k^i - \Phi_j^i)) P(\Phi_k^i) P(\Phi_j^i). \quad (29)$$

We start the analysis of the inspiral signal by constraining the angles in each of the i th segment of the signal. In order to do so, we consider the first set of data D_1 for the i th segment to be $D_{1i} \equiv (\rho_{21}^i, \rho_{31}^i, \Phi_{21}^i, \Phi_{31}^i)$. We use the Bayes theorem in each segment to obtain the constraints on the position in the sky and on the polarization and inclination angles. For $\Omega_{\text{sky}} \equiv (\delta, \alpha)$, $\Omega_{\text{source}} \equiv (t, \psi)$, we have

$$P(\Omega_{\text{eff}}|D_{1i}, I) = \frac{P(\Omega_{\text{eff}}|I)P(D_{1i}|\Omega_{\text{eff}}, I)}{P(D_{1i}|I)}, \quad (30)$$

where $\Omega_{\text{eff}} \equiv (\Omega_{\text{sky}}, \Omega_{\text{source}})$. Since the prior probability $P(\Omega_{\text{eff}}|I)$ is uniform on both the source and the detector sphere, we can write the prior probability as

$$P(\Omega_{\text{eff}}|I) = \frac{1}{(4\pi)^2} \quad (31)$$

and the likelihood as

$$\begin{aligned} P(D_{1i}|\Omega_{\text{eff}}, I) &= \int d\rho_{21}^i P(\rho_{21}^i) \int d\rho_{31}^i P(\rho_{31}^i) \\ &\times \int d\Phi_{21}^i P(\Phi_{21}^i) \int d\Phi_{31}^i P(\Phi_{31}^i) \\ &\times \delta(\rho_{21}^i - \rho_{21}^i(\Omega_{\text{eff}})) \delta(\rho_{31}^i - \rho_{31}^i(\Omega_{\text{eff}})) \\ &\times \delta(\Phi_{21}^i - \Phi_{21}^i(\Omega_{\text{eff}})) \delta(\Phi_{31}^i - \Phi_{31}^i(\Omega_{\text{eff}})). \end{aligned} \quad (32)$$

Given the information on the sky localization and source angles in the i th segment, we constrain Θ_{eff}^i by marginalizing over Ω_{eff} as

$$\begin{aligned} P(\Theta_{\text{eff}}^i|D_{1i}, I) &= \int d\Omega_{\text{eff}} P(\Theta_{\text{eff}}^i, \Omega_{\text{eff}}|D_{1i}, I) \\ &= \int d\Omega_{\text{eff}} P(\Omega_{\text{eff}}|D_{1i}, I) P(\Theta_{\text{eff}}^i|\Omega_{\text{eff}}, D_{1i}, I) \\ &= \int d\Omega_{\text{eff}} P(\Omega_{\text{eff}}|D_{1i}, I) P(\Theta_{\text{eff}}^i) \\ &\times \delta(\Theta_{\text{eff}}^i - \Theta_{\text{eff}}^i(\Omega_{\text{eff}})). \end{aligned} \quad (33)$$

We assume that

$$P(\Theta_{\text{eff}}^i) = \frac{1}{\Delta\Theta_{\text{eff}}^{\text{max}}}, \quad (34)$$

where $\Theta_{\text{eff}}^{\text{max}} = 6$. This is so because, for each of the three detectors in the ET, the angle between the interferometer arms is 60° . We can thus rewrite Eq. (33) as

$$\begin{aligned} P(\Theta_{\text{eff}}^i|D_{1i}, I) &= \frac{1}{\Delta\Theta_{\text{eff}}^{\text{max}}} \int d\Omega_{\text{eff}} P(\Omega_{\text{eff}}|D_{1i}, I) \\ &\times \delta(\Theta_{\text{eff}}^i - \Theta_{\text{eff}}^i(\Omega_{\text{eff}})). \end{aligned} \quad (35)$$

Substituting Eq. (30) in Eq. (35) gives the probability density for Θ_{eff}^i . Moving further, by rearranging Eq. (22), we notice that

$$\frac{\Theta_{\text{eff}}^i \sqrt{\zeta^i(f_{i-1}, f_i)}}{\rho_{\text{eff}}^i} \approx \left(\frac{8r_0}{D_L} \left(\frac{\mathcal{M}_z}{\mathcal{M}_{\text{BNS}}} \right)^{5/6} \right)^{-1}. \quad (36)$$

It is seen that, while the quantities Θ_{eff}^i , $\zeta^i(f_{i-1}, f_i)$, and ρ_{eff}^i on the lhs of Eq. (36) are individually measured depending on the segment characteristic for each segment, the rhs is characterized by the source. So we can define this as a source-dependent quantity Λ . Then, for each segment,

$$\Lambda \equiv \left(\frac{8r_0}{D_L} \left(\frac{\mathcal{M}_z}{\mathcal{M}_{\text{BNS}}} \right)^{5/6} \right)^{-1} \approx \frac{\Theta_{\text{eff}}^i \sqrt{\zeta^i(f_{i-1}, f_i)}}{\rho_{\text{eff}}^i}. \quad (37)$$

Here, $0 < \zeta^i(f_{i-1}, f_i) < 1$ and $0 < \Theta_{\text{eff}}^i < 6$; therefore, $0 < \Lambda^i < 6/\rho_{\text{eff}}^i$.

In order constrain this quantity Λ , we now take into account the second set of observed data D_2 for the i th segment, $D_{2i} \equiv (\rho_{\text{eff}}^i)$. Then the distribution of probability for Λ in the i th segment can be written as

$$P(\Lambda|D_{1i}, D_{2i}, I) = \int d\Theta_{\text{eff}} P(\Lambda, \Theta_{\text{eff}}|D_{1i}, D_{2i}, I). \quad (38)$$

The integrand can be expanded as

$$\begin{aligned} P(\Lambda, \Theta_{\text{eff}}|D_{1i}, D_{2i}, I) &= P(\Theta_{\text{eff}}|D_{1i}, D_{2i}, I) \\ &\times P(\Lambda|\Theta_{\text{eff}}, D_{1i}, D_{2i}, I) \\ &= P(\Theta_{\text{eff}}|D_{1i}, I) \\ &\times P(\Lambda|\Theta_{\text{eff}}, D_{1i}, D_{2i}, I), \end{aligned} \quad (39)$$

where the probability $P(\Theta_{\text{eff}}|D_{1i}, I)$ is obtained in Eq. (35) and

$$\begin{aligned} P(\Lambda|\Theta_{\text{eff}}, D_{1i}, D_{2i}, I) &= \int d\rho_{\text{eff}}^i P(\rho_{\text{eff}}^i) \\ &\times \delta(\Lambda - \Lambda(\Theta_{\text{eff}}^i/\rho_{\text{eff}}^i)), \end{aligned} \quad (40)$$

where

$$P(\rho_{\text{eff}}^i) = \int d\rho_1^i \int d\rho_2^i \int d\rho_3^i P(\rho_1^i) P(\rho_2^i) P(\rho_3^i) \times \delta\left(\rho_{\text{eff}}^i - \sqrt{(\rho_1^i)^2 + (\rho_2^i)^2 + (\rho_3^i)^2}\right). \quad (41)$$

Equations (30) and (38) give the probability distributions using information from the i th segment. Combining the information for all n segments, we can write

$$P(\Omega_{\text{eff}}|D_1, I) = \frac{1}{N_\Omega} \prod_{i=1}^n P(\Omega_{\text{eff}}|D_{1i}, I) \quad (42)$$

and

$$P(\Lambda|D_1, D_2, I) = \frac{1}{N_\Lambda} \prod_{i=1}^n P(\Lambda|D_{1i}, D_{2i}, I), \quad (43)$$

where N_Ω and N_Λ are normalization constants and $D_2 \equiv (\rho_{\text{eff}}^1, \rho_{\text{eff}}^2, \dots, \rho_{\text{eff}}^n)$, for all the n segments.

We can now impose constraints on the chirp mass and redshift of the source. We use the measured value of the redshifted chirp mass \mathcal{M}_z , and we assume that the measured probability density of the quantity $P(\mathcal{M}_z)$ is Gaussian with the width of $\sigma_{\mathcal{M}_z} = \mathcal{M}_z/\rho_{\text{eff}}$. Note that the justification of this assumption can be understood from Fig. 1 in Singh and Bulik [32]. We assume the error on f_{max} to be small enough to neglect it. In addition to Eqs. (13) and (19), we use the constraint implied by the definition of the chirp mass:

$$\frac{\mathcal{M}}{M} = \left[\frac{q}{(1+q)^2} \right]^{3/5} < 4^{-3/5}. \quad (44)$$

The last inequality in the above equation comes from the condition that $q_{\text{max}} = 1$. Then the joint probability of \mathcal{M} and z given this information I_Q is

$$P(\mathcal{M}, z|I_Q, I) = P(\mathcal{M}|I) P(z|I) \frac{P(I_Q|\mathcal{M}, z, I)}{P(I_Q|I)}, \quad (45)$$

where

$$P(I_Q|\mathcal{M}, z, I) = \mathcal{H}\left(\frac{\mathcal{M}}{2.8M_\odot} \frac{f_{\text{max}}(1+z)}{785 \text{ Hz}}\right) \times \mathcal{H}\left(4^{-3/5} - \frac{\mathcal{M}}{2.8M_\odot} \frac{f_{\text{max}}(1+z)}{785 \text{ Hz}}\right), \quad (46)$$

where $\mathcal{H}(x)$ is the Heaviside function.

We assume a flat cosmology with $\Omega_m = 0.3$, $\Omega_m + \Omega_\Lambda = 1$, $\Omega_k = 0$, and $H_0 = 67.3 \text{ km s}^{-1} \text{ Mpc}^{-1}$ [44]. The relation between the luminosity distance D_L and redshift z is obtained from the analytic approximation given by Adachi and Kasai [45]. The variation of comoving volume V with redshift z for this cosmology is

$$\frac{dV}{dz} = 4\pi D_H \frac{D_L^2}{(1+z)^2 E_z}, \quad (47a)$$

where

$$D_H = c/H_0 \quad \text{and} \quad E_z = \sqrt{\Omega_m(1+z)^3 + (1-\Omega_m)}. \quad (47b)$$

We assume flat priors on chirp mass \mathcal{M} , while the prior on redshift z comes from Eq. (47a) assuming that the rate density

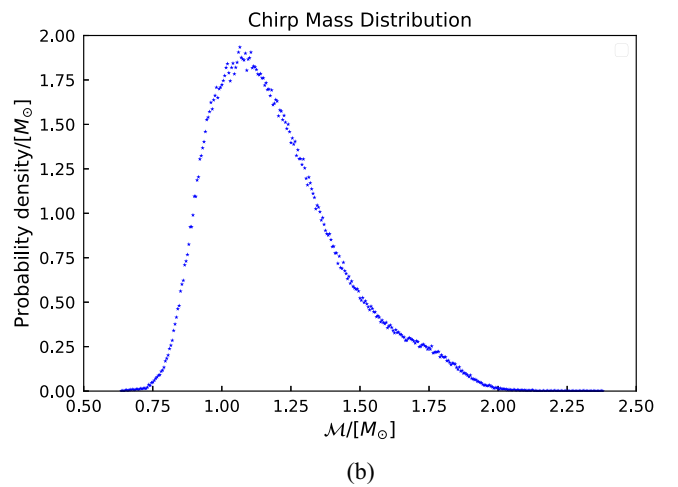
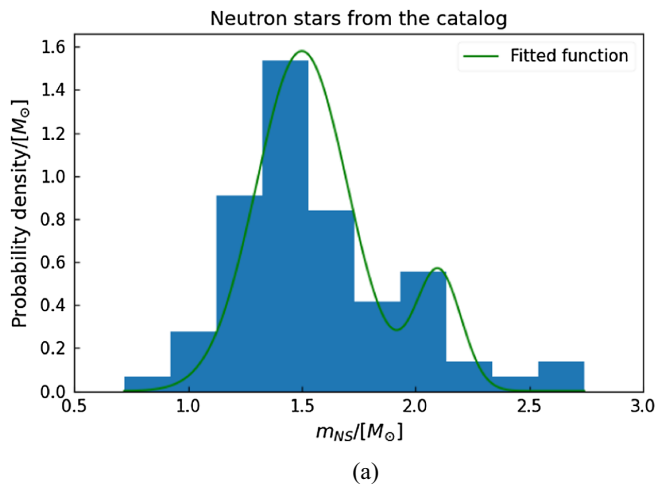


FIG. 1. The plots show the fit generated for the neutron star masses and the distribution of chirp masses of the sources in the mock catalog. (a) The probability distribution of neutron star masses mentioned in [49]. The green line is a summed Gaussian fit given in Eq. (60) for this distribution. The primary masses m_1 are drawn for using this fitting function and (b) The probability distribution for \mathcal{M} obtained for the low mass compact binary systems generated as mock sources using the distribution shown in (a).

of mergers per unit comoving volume per unit time is constant in the Universe. Therefore, we have

$$P(\mathcal{M}|I) = \frac{1}{(\mathcal{M}_{\max} - \mathcal{M}_{\min})} \quad (48)$$

and

$$P(z|I) = \frac{dV}{dz}. \quad (49)$$

We can now include the information on the measurement of the redshifted chirp mass and constraint on the quantity Λ to impose further constraint on \mathcal{M} and z . Taking into account the next observable $D_3 \equiv \mathcal{M}_z$, we can write

$$\begin{aligned} P(\mathcal{M}, z|D_1, D_2, D_3, I_Q, I) &\propto P(\mathcal{M}, z|I_Q, I) \iint d\Lambda d\mathcal{M}_z \\ &\times P(\Lambda|D_1, D_2, I) P(\mathcal{M}_z) \\ &\times \delta(\mathcal{M}_z - \mathcal{M}(1+z)) \\ &\times \delta(\Lambda - \Lambda(\mathcal{M}, z)), \end{aligned} \quad (50)$$

where we have used the form of Λ from Eq. (37) expressed in terms of \mathcal{M} and z , given as

$$\Lambda = \left(\frac{8r_0}{D_L(z)} \left(\frac{\mathcal{M}_z(\mathcal{M}, z)}{\mathcal{M}_{BNS}} \right)^{5/6} \right)^{-1}. \quad (51)$$

Substituting the prior $P(\mathcal{M}, z|I_Q, I)$ required in the above Eq. (50) from Eq. (45) as mentioned above, we obtain the joint probability of \mathcal{M} and z .

Taking $D' \equiv (D_1, D_2, D_3)$ and $I' \equiv I_Q, I$, the marginalized distribution for \mathcal{M} and z using Eq. (50) is given as

$$P(z|D', I') = \int d\mathcal{M} P(\mathcal{M}, z|D', I') \quad (52)$$

and

$$P(\mathcal{M}|D', I') = \int dz P(\mathcal{M}, z|D', I'). \quad (53)$$

The probability distribution for luminosity distance is obtained from the redshift using the cosmological assumptions described in Sec. IV:

$$\frac{dP}{dD_L} = \frac{dP}{dz} \frac{dz}{dD_L}. \quad (54)$$

Then we constrain the mass ratio using Eqs. (13) and (44) to express the mass ratio as a function of \mathcal{M} and z :

$$q(\mathcal{M}, z) = \frac{\xi}{2} - 1 - \sqrt{\frac{\xi^2}{4} - \xi}, \quad (55)$$

where

$$\xi = \left(\frac{785 \text{ Hz } 2.8M_\odot}{f_{\max} \mathcal{M}_z} \right)^{5/3}. \quad (56)$$

Now we can write

$$P(q|D', I') = \iint d\mathcal{M} dz P(\mathcal{M}, z, q|D', I'). \quad (57)$$

We assume a flat prior on the mass ratio $P(q|I') = 1$, so

$$P(q|D', I') \propto \iint d\mathcal{M} dz P(\mathcal{M}, z|D', I') \delta(q - q(\mathcal{M}, z)). \quad (58)$$

Substituting Eq. (50) in Eq. (58) gives the probability density for mass ratio q . The total mass of the binary M is obtained by using the observed value of the frequency f_{\max} and the probability distribution of redshift z . We can get the probability density of M as

$$\frac{dP}{dM} = \int \frac{dP}{dz} \frac{dP}{df_{\max}} dz df_{\max} \delta(M - M(z, f_{\max})). \quad (59)$$

Thus, using the observed SNRs, phases, redshifted chirp mass, and f_{\max} , we have constrained the astrophysical parameters: chirp mass, redshift, and the luminosity distance as well as total mass and mass ratio for a compact binary system.

V. MOCK SOURCE CATALOG

We generate a mock population of low mass compact binaries for this analysis assuming that the distributions of masses, distances, locations in the sky, and polarizations are independent. The cosmological assumption are as explained in the previous section. We assume that the mass distribution is the same for all distances.

Such a population of compact binary sources, distributed uniformly in comoving volume, is not a realistic one, since it does not take into account the dependence of the star formation rate on redshift and also neglects the delays between formation and coalescence. The calculation using this assumption of sources distributed uniformly in comoving volume, is done for illustrative purposes so as to access the quality of the method employed for data analysis. We choose this simplified assumption for creating the mock population of low mass compact binary sources to study the biases, if any, seen in the recovery of the parameters and to get an estimate of the accuracy of the recovered parameters. We discuss the analysis of more realistic populations in the next paper in this series [46].

The probability distributions of angular distribution $\cos \delta$, α/π , $\cos i$, and ψ/π are assumed to be uncorrelated and are distributed uniformly over the range $[-1, 1]$. We generate sources spread in redshift range $[0.01, 1.0]$, assuming that the rate density of mergers per unit comoving volume per unit time is constant in the Universe.

ET will be able to detect BNS binaries of total masses $\sim 3M_\odot$ up to $z \sim (2-3)$ [25], but we restrict the sources to

redshift $z < 1$ so as to have a substantial number of sources crossing the detection threshold we set for the analysis.

The SNR for a given binary source in the mock population is calculated using the PSD $S_h(f)$, for the ET-D noise curve [14] obtained from Ref. [47]. We choose the following criterion to define a detection: a threshold value of accumulated effective SNR $\rho_{\text{eff}} > 8$ and the SNR for the i th segment in the j th detector $\rho_j^i > 3$ in at least one segment, for $j = (1, 2, 3)$ corresponding to the three ET detectors comprising single ET. The justification of choosing only the segments with $\rho_j^i > 3$ and a comparison of detection thresholds is described in the Appendix.

To get a mass distribution for the low mass binary mock population, we use a summed Gaussian fit to the masses in the catalog [48] to get the distribution of primary mass m_1 . The fitting function is

$$p(m_1) \propto (\mathcal{N}(1.5, 0.2^2) + 0.35 \times \mathcal{N}(2.1, 0.1^2)), \quad (60)$$

where $\mathcal{N}(\mu, \sigma^2)$ denotes the normal distribution with the mean μ and standard deviation σ . The fit is shown in Fig. 1(a). The minimum and maximum mass limits for the binary components are restricted to $m_1, m_2 > m_{\text{min}}^{\text{NS}} = 0.72M_\odot$ and $m_1, m_2 < 2.74M_\odot$ in agreement with the values in the catalog. The mass ratio $q = m_2/m_1$ is chosen uniformly from the range $[m_{\text{min}}^{\text{NS}}/m_1, 1]$. The values of m_1 and m_2 then give the distribution of chirp mass \mathcal{M} of the mock population. This distribution of \mathcal{M} in this population is shown in Fig. 1(b).

VI. RESULTS

In our analysis, we consider only the inspiral part of the signal from coalescing low mass binaries. The sources which cross the detection threshold are taken up for the analysis. These are referred to as the detected *sources* in the discussion hereafter, and their parameters are denoted by subscript s . The signal from each detection is split into 5-min segments as described in Sec. IV, assuming that the change in the antenna response functions is negligible during that period. For each segment, we generate a four-dimensional space of $\cos \delta$, α/π , $\cos \iota$, and ψ/π , randomly distributed uniformly over the range $[-1, 1]$. This 4D grid is constrained using Eqs. (26) and (27) to get a distribution of Ω_{eff} from Eq. (30). This gives us the sky localization of declination and right ascension (δ, α) on the celestial sphere and constraint on the source angles (ι, ψ) . Since we

assumed that the antenna response functions remain unchanged during 5 min, this introduces a systematic error in the location which is smaller than 1.25° . In order to avoid dealing with this potential contribution to the localization error, we keep the bin size of the sphere to be 1.28 square degrees.

We get the posterior distribution of Θ_{eff}^i from Eq. (35) for each segment using the information obtained for Ω_{eff} . Since we assume that the effective SNR ρ_{eff}^i is known for each segment in the three ET detectors, we use this information about the measured values of ρ_{eff}^i and the distribution of Θ_{eff}^i obtained in each segment to provide a constraint on Λ , given by Eq. (38). The function Θ_{eff}^i varies for each segment as the antenna response function changes with the rotation of Earth. $\zeta^i(f_{i-1}, f_i)$ varies due to change in the limit of integration as specified in Eq. (20). From Eq. (37), we see that Λ , is a source-dependent quantity. This process is repeated for all the segments, and the final distribution for Ω_{eff} and Λ is obtained by combining information obtained from all the segments as given by Eqs. (42) and (43).

In order to estimate the other parameters of the binary system, we construct a 2D grid for redshift z and chirp mass \mathcal{M} , with ranges from $0.005 \leq z \leq 1.5$ and $0.6 \leq \mathcal{M}/M_\odot \leq 2.5$. The limits of these ranges extend beyond the limits of the mock sources so that the sources at the edge of the mock population can be recovered correctly. The prior on z is given by Eq. (49) with details given in Sec. IV. The prior on \mathcal{M} is assumed to be flat, given by Eq. (48).

Since we assume that the redshifted chirp mass is known from match filtering, we use this information to select the appropriate values from the 2D (z, \mathcal{M}) grid. The observed value of f_{max} , the frequency at the end of the inspiral, gives the information about the mass ratio q which further limits the valid grid points. Last, since we have a distribution of Λ , obtained by combining information from all the detected segments, we use this distribution to get the joint probability of (z, \mathcal{M}) using Eq. (50). The distributions for luminosity distance D_L and mass ratio q are obtained from Eqs. (54) and (58), respectively, and the distribution for total mass M is obtained using Eq. (59). The subscript “*median*” represents the median value of these distributions obtained for the parameters of the binary system.

A. Analysis of particular cases

To demonstrate the method described above, we discuss two cases. The details of the two cases are mentioned in Table I. In case 1, we consider a low mass compact binary

TABLE I. Details of two cases discussed in Sec. VI A. The SNR values mentioned here are the accumulated SNRs in each of the three detectors.

	ρ_1	ρ_2	ρ_3	ρ_{eff}	$\mathcal{M} (M_\odot)$	$M (M_\odot)$	z	D_L (Gpc)	q	$(\cos \delta, \alpha, \cos \iota, \psi)$
Case 1	8.94	5.30	7.11	12.59	1.16	2.71	0.44	2.53	0.71	(−0.76, 3.72, −0.73, 5.90)
Case 2	18.16	24.70	41.56	51.64	1.68	3.91	0.1	0.47	0.74	(0.07, 1.29, −0.59, 4.35)

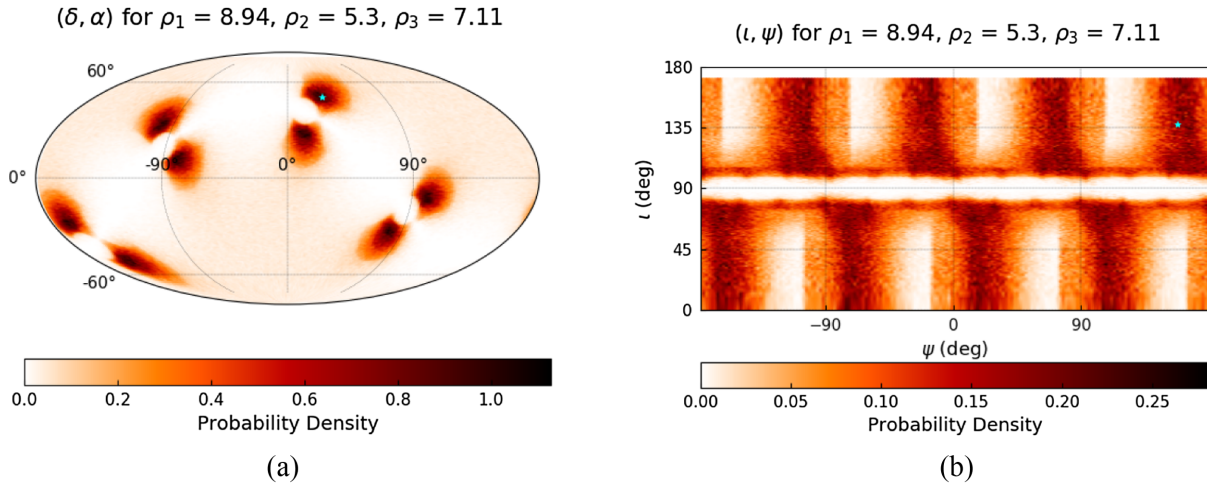


FIG. 2. The final probability distribution for (δ, α) (a) and (ι, ψ) (b) obtained for Case 1. The signal is detectable in the band for only one segment for a duration of 1.38 minutes. The blue star in the plots denotes the actual source parameters.

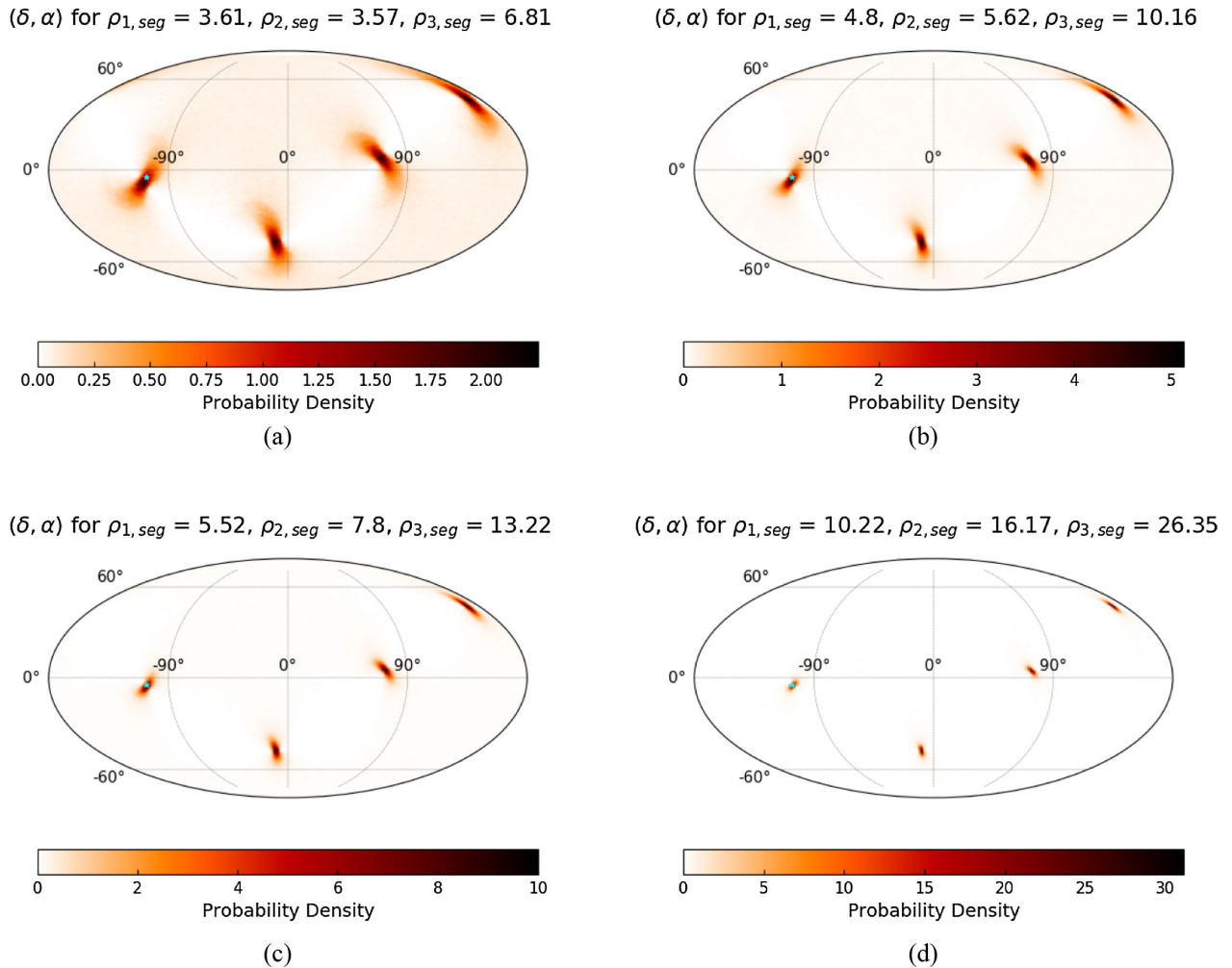


FIG. 3. Localization in each segment for case 2. Plots shown here are for the (a) first, (b) third, (c) fifth, and (d) last seventh segment from the time the signal crosses the threshold of detection up till the last segment. There are seven segments, as the signal is 30.63 min long in this case. Going from $a \rightarrow b \rightarrow c \rightarrow d$ shows the distributions obtained successively in time for the declination and right ascension (δ, α) . The SNR values $\rho_{j,seg}$ denote the SNR generated in the particular segment of the j th detector. The blue star denote the actual value of declination and right ascension (δ, α) of the detected source on the celestial sphere.

system with chirp mass $\mathcal{M} = 1.16M_{\odot}$, total mass $M = 2.71M_{\odot}$ located at redshift $z = 0.44$. The inspiral signal from this binary enters the ET band at 1 Hz but is detected only at the start of the 924th segment. In this segment, $(f_{i-1}, f_i) \sim (20.95, 1128.07)$ Hz. The SNR values in this segment cross the detection threshold with $\rho_{1,\text{seg}} = 8.94$, $\rho_{2,\text{seg}} = 5.30$, and $\rho_{3,\text{seg}} = 7.11$. Since this is the last segment of the inspiral signal for this binary, we have the information from this one segment only, which is 1.38 min long. The distributions for declination, right ascension (δ, α) and inclination, polarization angle (ι, ψ) are shown in Fig. 2. In the distribution for (δ, α) , we see the degeneracy in the recovered angles coming from the nature of dependence of Θ function on the angles. In particular, there is the symmetry about the equatorial plane, i.e., $(\theta \rightarrow -\theta)$, and also with respect to the rotation by 90° about the longitude, i.e., $(\phi \rightarrow \phi + 90^\circ)$, where (θ, ϕ) are the sky coordinates in the detector frame (see Fig. 2 in Ref. [32] for a better understanding). This results in eight images of possible locations of the source. The plot shown in Fig. 2(a) shows the localization of (δ, α) is fairly well constrained, while the constraint on (ι, ψ) as seen in Fig. 2(b) is much weaker. The area of 90% probability (A_{90}) about the peak for declination and right ascension (δ, α) in this case is 2.02×10^4 square degrees.

Case 2 is a detected source with $\mathcal{M} = 1.68M_{\odot}$, total mass $M = 3.91M_{\odot}$ located at redshift $z = 0.1$. After entering the ET band at 1 Hz, the signal is detected in the 775th segment. In this first detected segment, $\rho_{1,\text{seg}} = 3.61$, $\rho_{2,\text{seg}} = 3.57$, and $\rho_{3,\text{seg}} = 6.81$ in the three ET detectors and $(f_{i-1}, f_i) \sim (6.16, 6.58)$ Hz. For this case, the inspiral signal stays for 30.63 min in the detectable range of ET, with a total of seven segments. In the last segment,

$(f_{i-1}, f_i) \sim (26.47, 1023.35)$ Hz. The plots in Fig. 3 show first, third, fifth, and the final seventh segment from the time the signal crosses the threshold of detection. Moving from 3(a) \rightarrow 3(b) \rightarrow 3(c) \rightarrow 3(d), we can see the reduction in the area of localization in each segment with an increase in ρ_{eff} for each segment. We combine the probabilities from all these segments to get the final probability shown in Fig. 4. The main advantage of combining the information from all the segments in this manner is the breaking of the angular degeneracy. Now, instead of a large spread of possible localization of the source, we have a much smaller region left, spread over only four images. The area of 90% probability about the peak for declination and right ascension (δ, α) in this case is 38.41 square degrees.

We use the observed value of redshifted chirp mass \mathcal{M}_z to limit the initial 2D grid of redshift z and chirp mass \mathcal{M} to those which satisfy this observed value within the error of measurement $\sigma_{\mathcal{M}_z}$. The observable f_{max} , the frequency at the end of the inspiral, gives the information about the mass ratio q restricting the grid even more using Eq. (45). We get the final distribution for the joint probability distribution for z and \mathcal{M} , using the distribution for Λ from Eq. (50).

The distributions obtained for \mathcal{M} and z for case 1 and case 2 are shown in left and right panels, respectively, in Fig. 5. Figures 5(a) and 5(b) are the joint probabilities for \mathcal{M} and z obtained using Eq. (50). Figures 5(c) and 5(d) show the marginalized probability distribution recovered for the redshift z . The 90% error about the median of the recovered redshift decreases from 0.36 for case 1 to 0.04 for case 2. Figures 5(e) and 5(f) show the marginalized probability distribution for \mathcal{M} for which the error about the median reduces from $0.35M_{\odot}$ to $0.13M_{\odot}$. Figure 6 shows

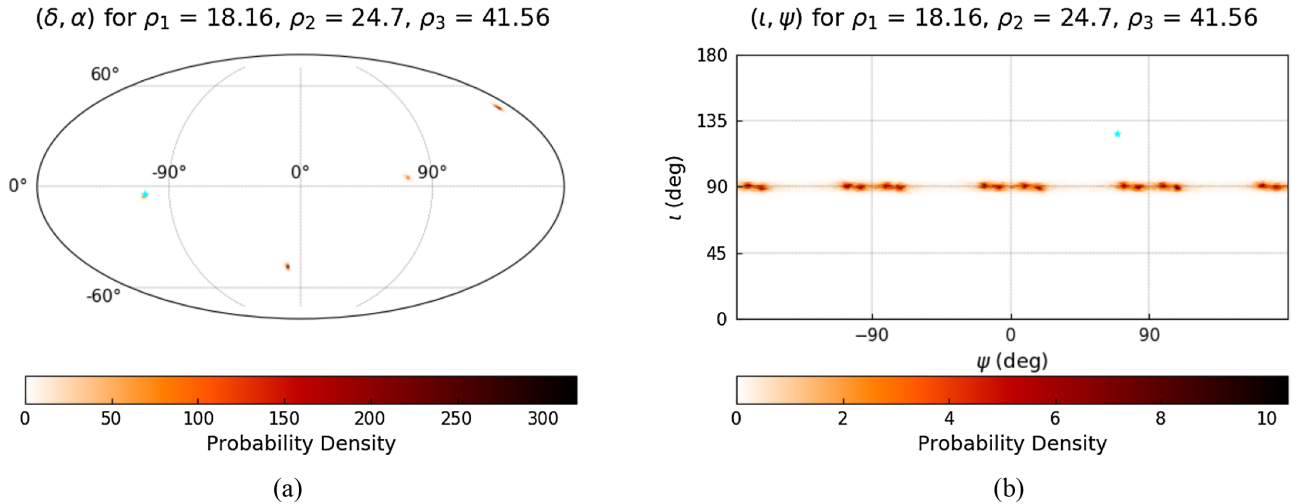


FIG. 4. The (a) shows the final probability distribution for (δ, α) obtained for case 2 by combining probabilities for all the segments (some of which are shown in Fig. 3). The corresponding final probability of (ι, ψ) is shown in the (b). The SNR values denote the accumulated SNRs in each detector. The blue star denote the declination and right ascension (δ, α) value of the detected source on the celestial sphere.

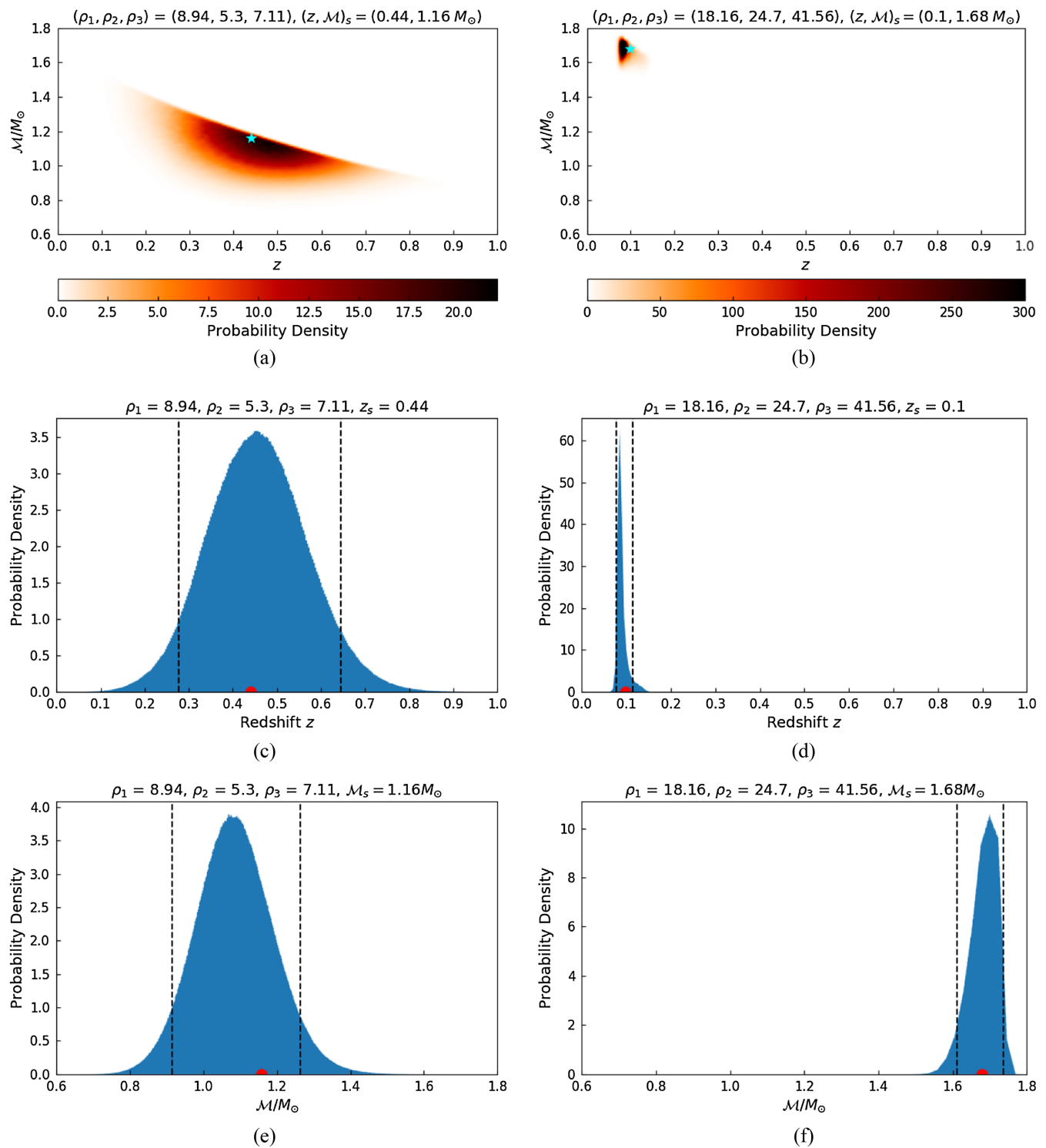


FIG. 5. The distributions obtained for \mathcal{M} and z for case 1 (left) and case 2 (right). The top panel shows the joint probability of \mathcal{M} and z . The marginalized probabilities of these quantities are shown in the lower panels. The blue star in the top panel plots and red dot in the middle and bottom panel plots denote the actual source value of the parameters.

the corresponding distributions of luminosity distance D_L and mass ratio q and total mass M for case 1 and case 2. The values of the error estimates for all the parameters are mentioned in Table II.

B. Analysis of mock population

We generate a 2D grid of 80 000 points for (m_1, q) using Eq. (60) and choosing the mass ratio to be uniformly distributed in the range $[m_{\min}^{NS}/m_1, 1]$. We then

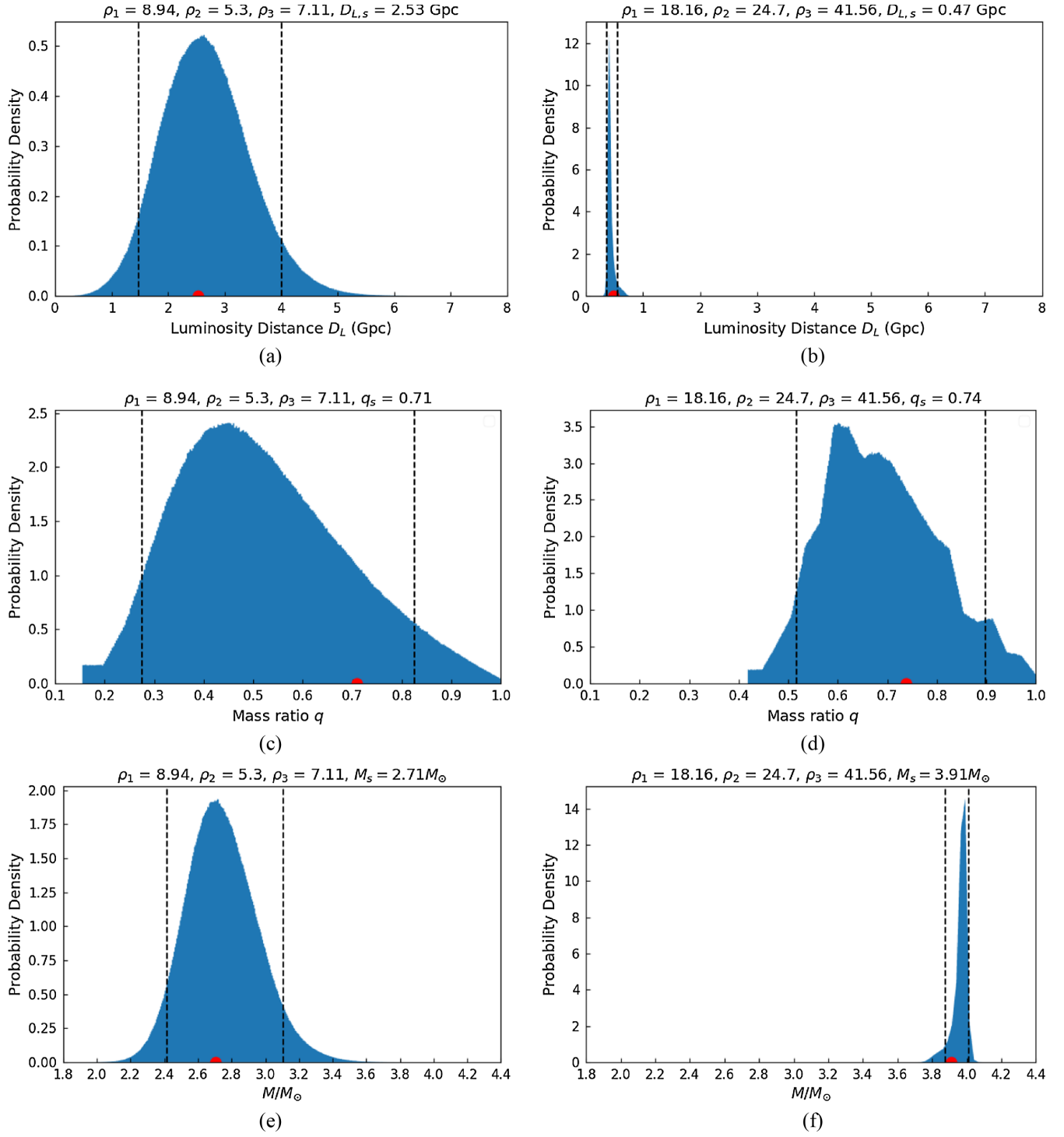


FIG. 6. The distribution of luminosity distance D_L (a,b), mass ratio q (c,d), and total mass M (e,f), for case 1 (left) and case 2 (right). The red dot denotes the actual source value of the parameter.

apply the limits on m_1, m_2 as discussed in Sec. V. After applying these cuts, we are left with 42 514 binary sources which are then randomly distributed in redshift using Eq. (49). Each compact binary system is then assigned a set of random values of the four angles: angle of declination δ , right ascension α , polarization angle ψ , and inclination

angle ι of the binary with respect to the direction of observation.

Out of these 42 514 sources, 17 994 compact binary systems cross the detection threshold and are taken up for the analysis. We discuss the localization and constraints on the binary parameters in the following sections.

TABLE II. Errors on the recovered values for the two cases mentioned in Table I. The error on the parameters is the estimate for the spread of 90% probability about the median for the respective parameters. The area estimated for the localization of declination and right ascension, (δ, α) is the spread for 90% probability about the peak value of the (δ, α) distribution.

	$\Delta\mathcal{M} (M_\odot)$	$\Delta M (M_\odot)$	Δz	ΔD_L (Gpc)	Δq	Area for (δ, α) localization (A_{90}) (sq deg)
Case 1	0.35	0.69	0.36	2.49	0.55	2.02×10^4
Case 2	0.13	0.16	0.04	0.20	0.37	38.41

1. Localization capability

The distribution of sky localization using a single ET is shown in Fig. 7. The sources are assumed to be distributed uniformly in comoving volume. It shows the cumulative distribution of area of 90% probability, A_{90} of the sky localization. The two dashed lines in this figure denote the 50% and 90% cumulative probability. 100% of the analyzed sources distributed uniformly in comoving volume are localized within $\sim 2.90 \times 10^4$ square degrees which is $\sim 70\%$ of the whole sky. 90% of the analyzed sources are localized within $\sim 2.55 \times 10^4$ and 50% are within $\sim 2.23 \times 10^4$ square degrees. For the best case, we see that using this method of analyzing the long-duration signal, single ET in triangular configuration can constrain the localization area for 90% probability region of (δ, α) to a minimum value of 7.68 square degrees, for $\rho_{\text{eff}} = 184.59$, but only $\approx 1\%$ of binaries can be localized within 800 square degrees.

The dependence of sky localization on the effective SNR is shown in Fig. 8(a). It shows that, for the sources which have inclination $\iota < 70^\circ$ or $\iota > 110^\circ$, the area of sky localization decreases exponentially with the effective SNR, while only a small fraction of sources having $70^\circ < \iota < 110^\circ$ are detectable. We investigated different cutoffs in the inclination angle and found that, given the

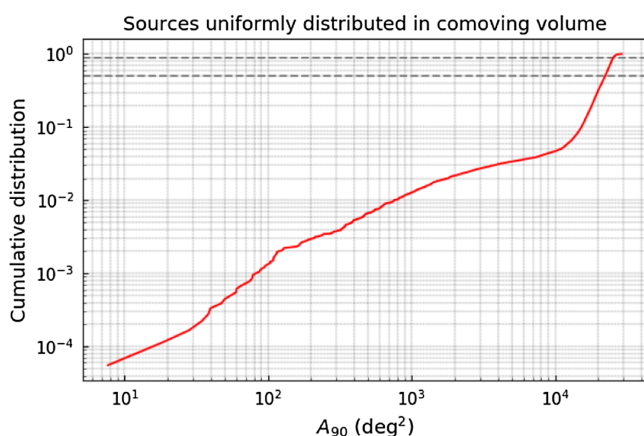


FIG. 7. Localization of the sources distributed uniformly in comoving volume using single ET. The figure shows the cumulative distribution of 90% probability about the peak for (δ, α) . The two dashed lines denote the 50% and 90% cumulative probability.

low SNR values, the sources with $70^\circ < \iota < 110^\circ$ have much poorer localization. No such dependence of sky localization on angle of declination, right ascension, or angle of polarization δ, α, ψ was seen. Figures 8(b) and 8(c) show that in the mass range of the detected population, irrespective of value of the inclination angle and the chirp mass, only the sources located at $z \lesssim 0.15$ can be localized within a 90% credible region of 1000 square degrees.

2. Mass and distance estimates

In this analysis, we recover the probability distributions for chirp mass \mathcal{M} , redshift z , luminosity distance D_L , and mass ratio q for 17 994 detected sources in addition to their angular distributions. The relative error on the parameters are estimated from the spread of 90% probability about the median of the recovered distributions for the respective parameters.

Figure 9 shows the distribution of relative error on the parameters of the detected compact binary system with the accumulated effective SNR. We see that the relative error drops with increasing ρ_{eff} . For \mathcal{M} it reduces from $\sim 20\%$ at $\rho_{\text{eff}} \sim 15$ to $\sim 5\%$ at $\rho_{\text{eff}} \sim 50$. Figure 9(b) shows that the relative error redshift goes down from $\sim 40\%$ at $\rho_{\text{eff}} \sim 15$ to $\sim 15\%$ at $\rho_{\text{eff}} \sim 50$. The respective errors for total mass M , luminosity distance D_L , and mass ratio q are shown in Figs. 9(c), 9(d), and 9(e), respectively.

3. The effect of inclination on the recovery of parameters

The discussion in the previous section showed that sky localization has a dependence on the inclination angle ι of the detected compact binary system. It was shown in Fig. 8 that, for the detected compact binary sources located at $z \gtrsim 0.15$, the sources with $70^\circ < \iota < 110^\circ$ have a poor localization given the low SNR value. In addition to this, Fig. 10 shows the distribution of relative errors on \mathcal{M} and z for all the detected sources with the sky localization. The left panels in Figs. 10(a) and 10(b) show the sources with $\iota < 70^\circ$ or $\iota > 110^\circ$, and the right panels show the sources with $70^\circ < \iota < 110^\circ$. It can be seen that, although only a few sources with $70^\circ < \iota < 110^\circ$ generate enough SNR to be detected, the accuracy of recovered values of \mathcal{M} and z for these low-SNR cases, i.e., $A_{90} > 23 \times 10^3$ square degrees, is better than for those with $\iota < 70^\circ$ or $\iota > 110^\circ$. Most of the sources detectable with higher SNR and having better localization are the sources with the inclination angles $\iota < 70^\circ$ or $\iota > 110^\circ$.

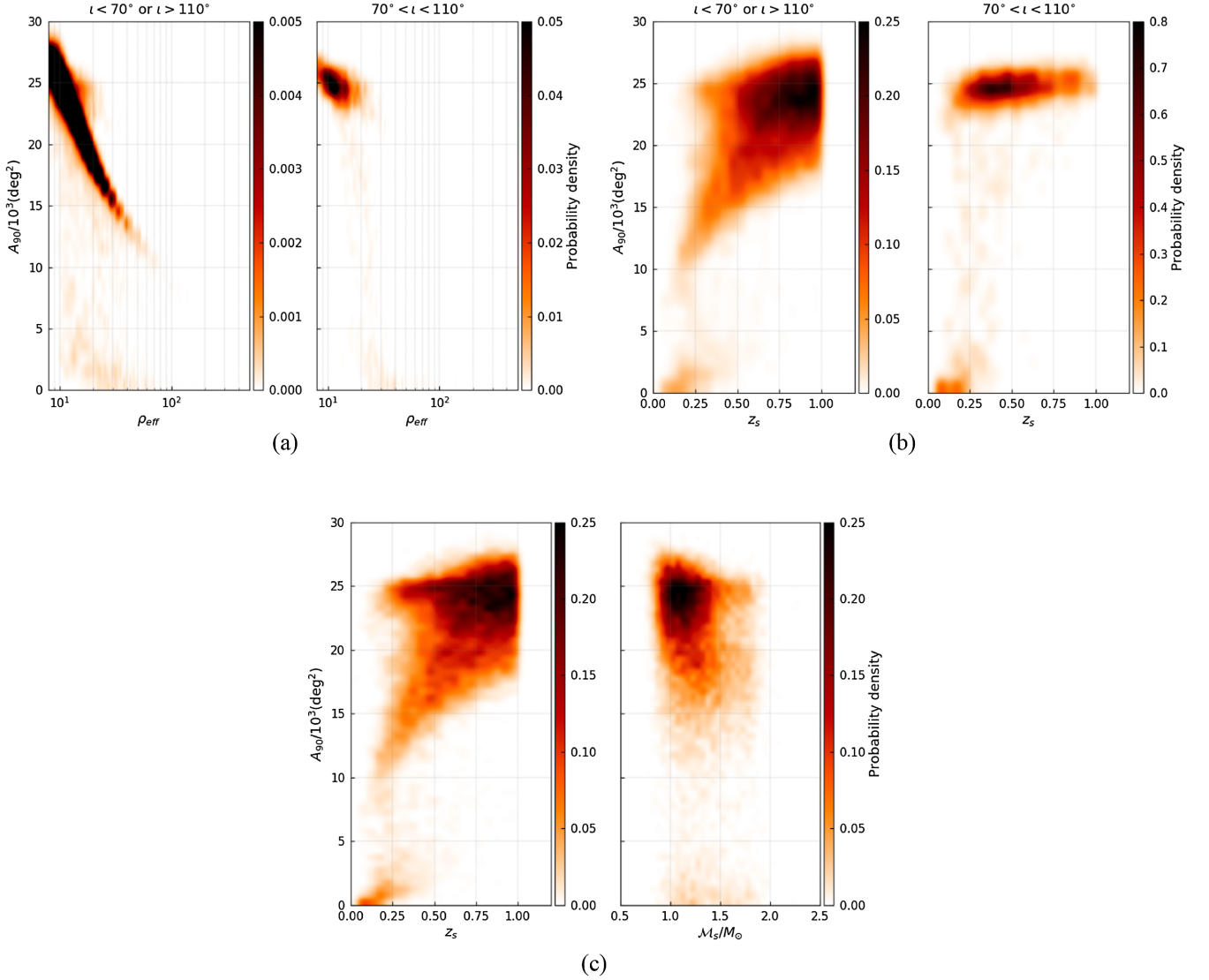


FIG. 8. The dependence of sky localization on ρ_{eff} and redshift is shown in (a) and (b) for two sets of inclination angles, ($\iota < 70^\circ$ or $\iota > 110^\circ$) and ($70^\circ < \iota < 110^\circ$). The dependence of sky localization on redshift and chirp mass for all the detected sources is shown in (c).

4. The effect of choice of site on the localization capability of ET

We now proceed to test the localization capability of the ET for different orientations and at different sites. In order to see the affect of orientation of the detector on the sky localization, we assume that the ET is located at the Virgo site and repeat the analysis using the ET detector with three different orientations. The orientation γ is measured counterclockwise from East to the bisector of the interferometer arms. We assume the initial orientation to be $\gamma = 84.84^\circ$ and then analyze the same set of detected sources with the ET detector orientated at $\gamma_1 = \gamma + 30^\circ$ and $\gamma_2 = \gamma + 60^\circ$. Figure 11(a) shows the cumulative distribution of sky localization for these three different cases of orientation of the detector at the Virgo site. It can be

concluded that the change in orientation does not have much effect on the sky localization.

We also investigate the change in the sky localization for different site locations of ET. We assume the locations to be in Maastricht and Sardinia in addition to the Virgo site. The coordinates of the sites are mentioned in Table III. The site locations are chosen keeping in mind that these are the official candidate sites for the ET. The cumulative distributions of sky localization for these locations are shown in Fig. 11(b) and show no change in the effective sky localization.

5. Biases in recovery of the parameters of the binary

In order to check the accuracy of the algorithm in recovering the distributions of the binary parameters, we

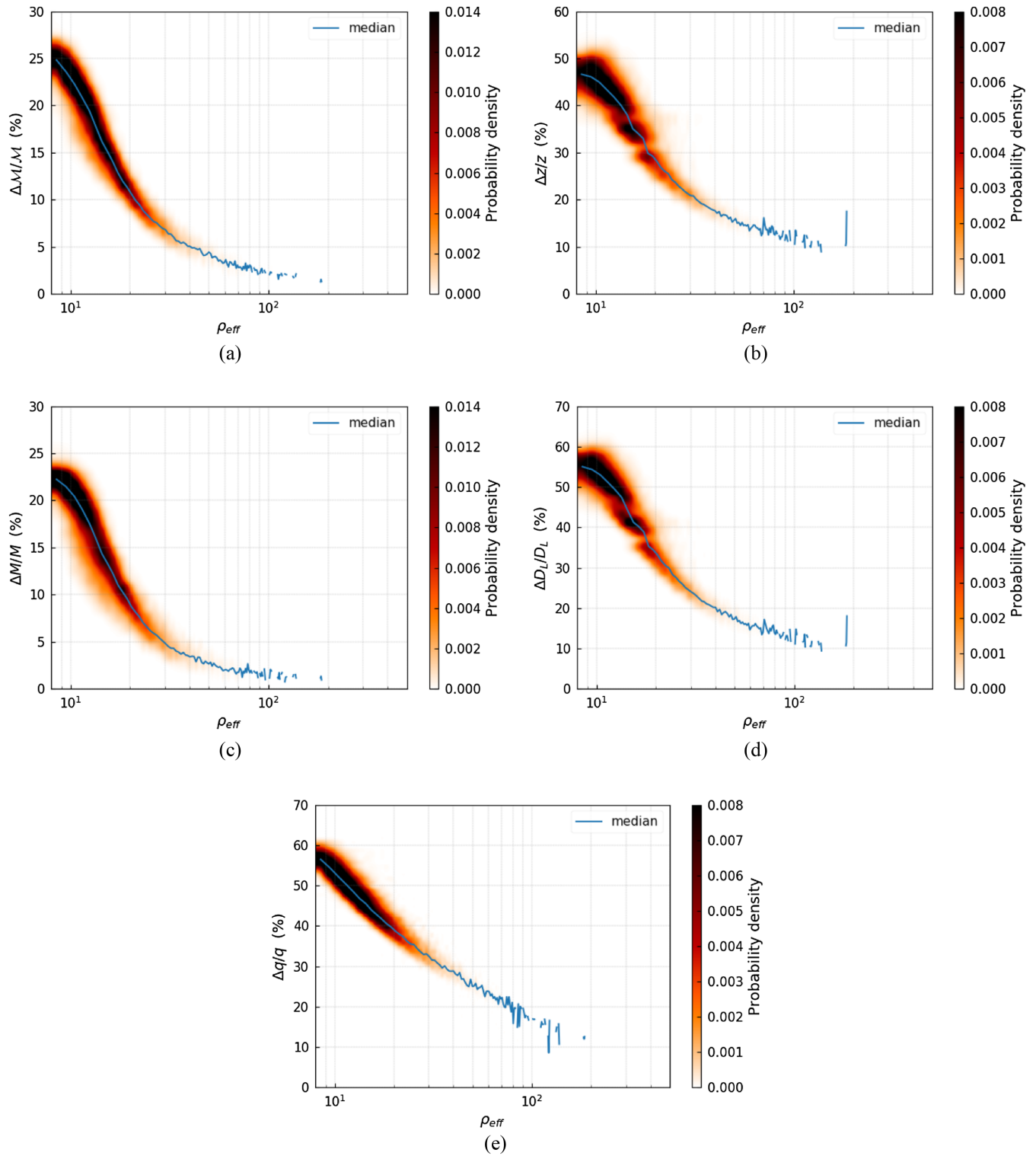


FIG. 9. Distribution of relative errors on (a) chirp mass \mathcal{M} , (b) redshift z , (c) total mass M , (d) luminosity distance D_L , and (e) mass ratio q , for all the detected sources, with ρ_{eff} . The relative error on the parameters are estimated from the spread of 90% probability about the median of the distribution of the respective parameters.

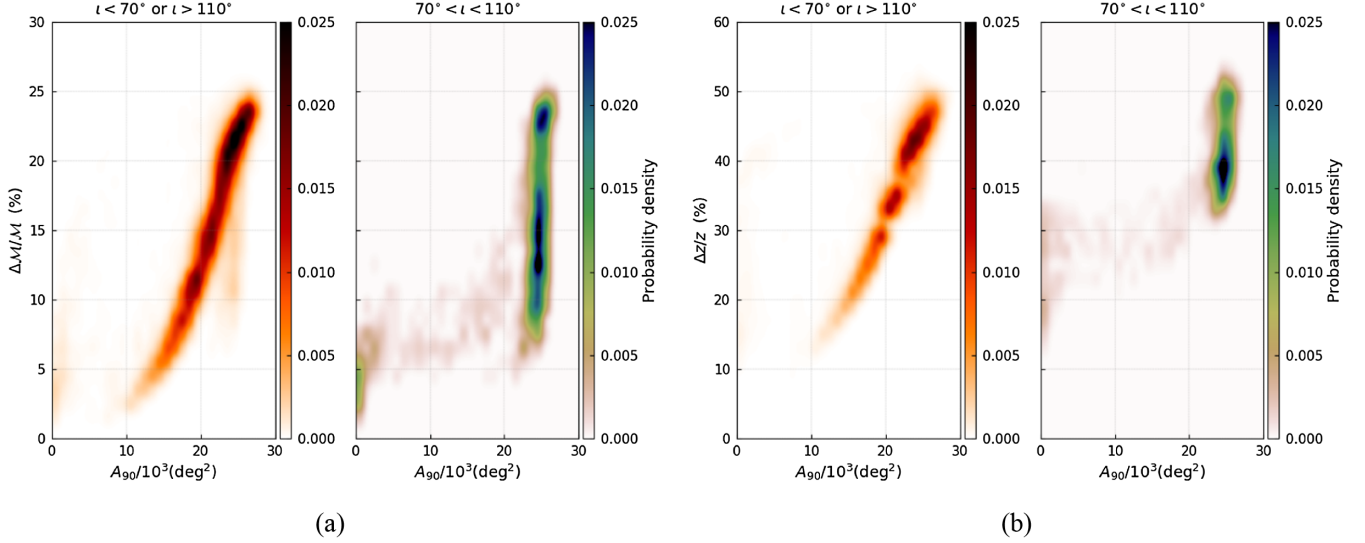


FIG. 10. Distribution of relative errors on (a) chirp mass \mathcal{M} and (b) redshift z for all the detected sources with respect to the sky localization for two sets of inclination angles, ($\iota < 70^\circ$ or $\iota > 110^\circ$) and ($70^\circ < \iota < 110^\circ$).

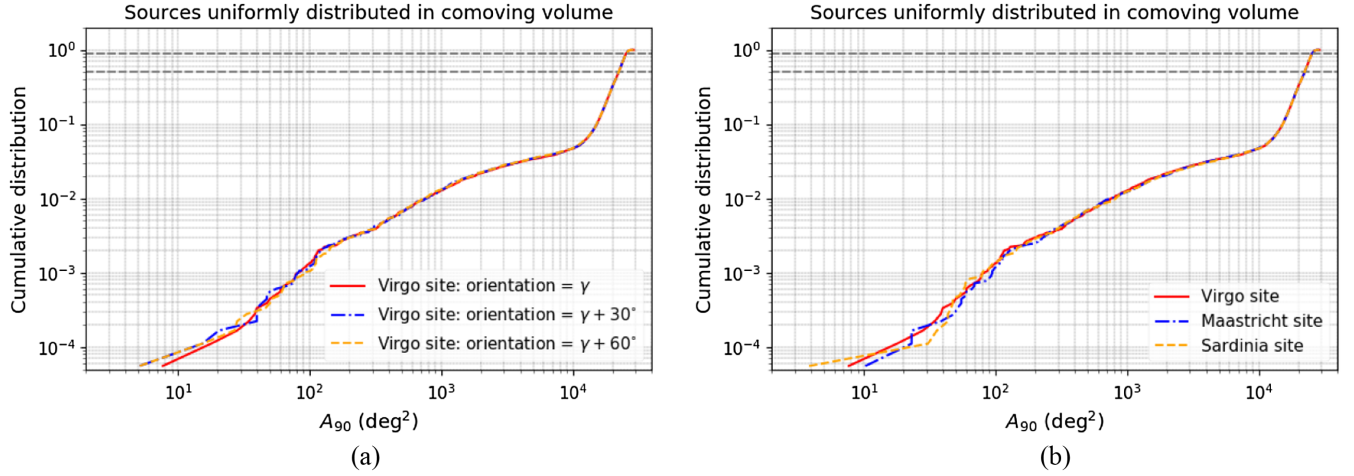


FIG. 11. Plot showing the effect of different site coordinates on the sky localization. (a) The change in the recovered sky localization with the change in the orientation of the ET detector located at the Virgo site. Assuming that the initial orientation of ET is γ , the plot compares the localization with that obtained for $\gamma + 30^\circ$ and $\gamma + 60^\circ$. (b) The recovered sky localization for Virgo, Maastricht, and Sardinia sites.

TABLE III. The assumed coordinates of the sites for the ET in this analysis. γ is measured counterclockwise from East to the bisector of the interferometer arms, and η is the angle between the interferometer arms.

	Latitude	Longitude	Orientation	Arm angle
Site for ET	λ	L	γ	η
Virgo	43.68°	10.49°	84.84°	60°
Sardinia	40.12°	9.01°	0°	60°
Maastricht	50.85°	5.69°	0°	60°

show the recovered median values of the distributions with respect to source values for chirp mass \mathcal{M} , redshift z , and total mass M in Fig. 12. The blue contour in the plots encloses the 90% probability region.

Figure 12(a) shows the distribution of recovered median values of the intrinsic chirp mass $\mathcal{M}_{\text{median}}$ with respect to the actual source value \mathcal{M}_s values. It is seen that the chirp masses are recovered correctly over the whole range of source values.

In the case of the median values of the redshift distribution, shown in Fig. 12(b), we see that all cases detected with $z \gtrsim 0.6$ are slightly underestimated. This can

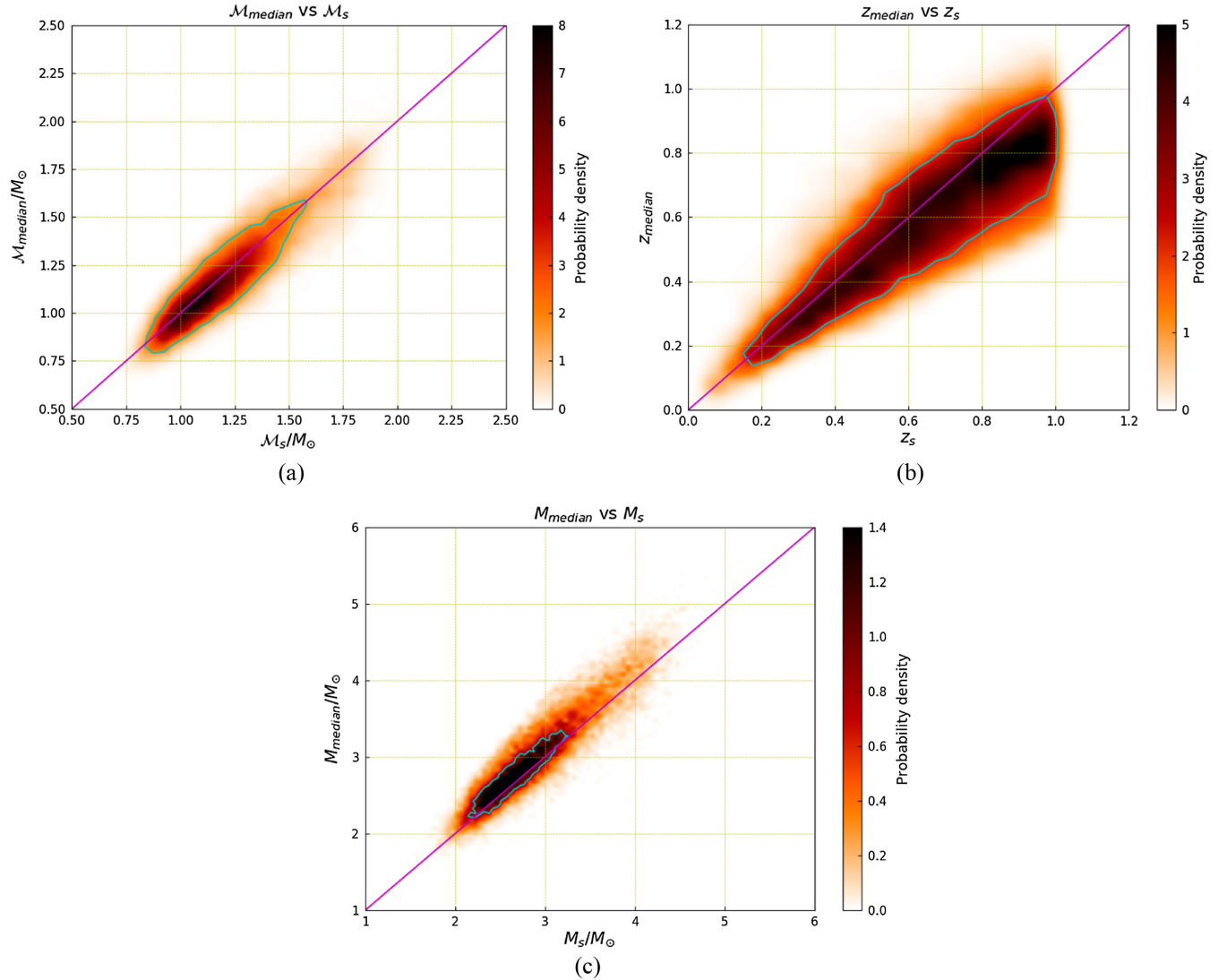


FIG. 12. The density distribution of the recovered median values of (a) \mathcal{M} , (b) z , and (c) M , with respect to the actual source values of the respective parameters. The purple lines represents the source = median reference line.

be explained due to the low SNR generated by these sources and, hence, the larger error associated with the SNR as per our prior assumption. A more detailed explanation of the origin of this bias is given in the Appendix.

Figure 12(c) shows the recovered median vs source value for the total mass M . We see that the recovered median values are overestimated over the whole range of source values. As mentioned earlier, we assume that f_{\max} , which gives the value of redshifted total mass, is measured accurately. Since redshift is underestimated, we see the overestimation in the recovered total mass M values.

VII. CONCLUSION

In this analysis, we studied the ability of ET as a single instrument to study longer-duration signals from coalescing low mass compact binary systems. We assume the detector

to be located at the Virgo site and analyze the signal every 5 min, assuming that the response functions for the three ET detectors do not change much within that period.

We show that, although one cannot use time of flight delays to constrain the position in the sky of a given source in case of three colocated detectors in single ET, combining information from different antenna patterns for each of the three detectors in each time segment provides good constraints on the parameters of a merging binary system.

We analyzed a mock population of compact binary sources for which the signal will stay for a long duration in the ET detection band. Assuming that the change in the response functions is negligible within 5 min, we divided the inspiral signal into 5-min segments from the time it enters the detection band of ET at 1 Hz with the duration of the last segment limited by f_{\max} , the frequency at the end of the inspiral.

We assumed the threshold of detection to be $\rho_j^i > 3$ for the i th segment in the j th detector in at least one segment, for $j = (1, 2, 3)$ corresponding to the three ET detectors comprising single ET and the accumulated SNR effective SNR $\rho_{\text{eff}} > 8$.

The angles describing the location of the source, its inclination, and polarization are constrained using the ratios of the SNRs generated in each signal segment of the three detectors of the equilateral triangle configuration of ET. This, in turn, provide constraints on the antenna response function Θ_{eff}^i in the i th segment.

We then use the information about Θ_{eff}^i and ρ_{eff}^i and initial and final GW frequency f_{i-1}, f_i in the i th segment to estimate the parameter Λ . Combining the information about the angles from each segment increases the accuracy of the estimate of the angles and also gives a stricter constraint on Λ . We then use the constraint on Λ to estimate intrinsic chirp mass \mathcal{M} , redshift z , total mass M , luminosity distance D_L , and mass ratio q of the merging binary system.

We conclude that the ET as a single instrument can localize the low mass compact binary sources and break the chirp mass–redshift degeneracy. The analysis presented here allows us to estimate source frame masses and redshifts of the coalescing compact binaries, which facilitates the population study of compact object binaries [46].

We find that the accuracy of determination of the redshift and the source frame chirp mass with ET as a single instrument is typically 40% and 20%, respectively, for $\rho_{\text{eff}} \sim 15$, and it is $\sim 15\%$ and $\sim 5\%$ for $\rho_{\text{eff}} \sim 50$. In the best case, we see that, using this method for analyzing a long-duration signal, single ET in triangular configuration can constrain the localization area for 90% probability region of (δ, α) to a minimum value of 7.68 square degrees, for $\rho_{\text{eff}} = 184.58$, although only $\approx 1\%$ of binaries can be localized with 90% credibility, within 800 square degrees. It should be noted that the dominant error in the analysis is the one on the SNRs and our assumption of $\sigma_\rho = 1$ is a conservative one.

We also studied the effect of orientation of the detector on the sky localization with three different orientations of ET detector assumed to be located at the Virgo site and found that the change in orientation has no effect on the sky localization. In addition to this, we also investigated the change in the sky localization for different site locations of ET. We assumed the location of ET to be in Maastricht and Sardinia in addition to Virgo and found no change in the effective sky localization due to change in the ET site for these sites.

ACKNOWLEDGMENTS

We acknowledge the support from the Foundation for Polish Science Grant No. TEAM/2016-3/19 and Narodowe Centrum Nauki Grant No. UMO-2017/26/M/ST9/00978. N.S. is supported by the “Agence Nationale de la

Recherche,” Grant No. ANR-19-CE31-0005-01 (PI: F. Calore). We thank the anonymous reviewer for all the valuable comments and suggestions which helped us to improve the manuscript. This document has been assigned Virgo document number VIR-0785A-21.

APPENDIX: EXPLANATION FOR THE BIAS IN PARAMETER ESTIMATION

In Fig. 12(a), we see the deviation of the median value of the parameter from the true value of that parameter. This origin of this *bias* can be understood from Fig. 13, which shows the distribution of Θ defined in Eq. (6), assuming that the probability distributions of angular distribution $\cos\delta$, α/π , $\cos i$, and ψ/π are uncorrelated and are distributed uniformly over the range $[-1, 1]$. We see that this distribution of Θ is inherently biased toward lower values. Therefore, for a given ρ , defined in Eq. (9), the smaller Θ has to be compensated by larger chirp mass \mathcal{M} and smaller redshift z . Thus, there is an inherent bias toward lower redshift and larger chirp mass.

One of the main building blocks of our analysis is that we use the ratios of SNRs in each segment for each of the three detectors in the triangular configuration of ET, to constrain the value of the effective antenna pattern. This is expressed in Eq. (26), assuming that the measurement error on the SNRs is Gaussian with the standard deviations for ρ_j^i being $\sigma_\rho = 1$. In Fig. 14, we show the absolute value of bias as the function of the ratio of the SNRs. We see that the estimate of parameters is likely to be biased for $\rho_2/\rho_1 \approx 1$ and $\rho_3/\rho_1 \approx 1$. The reason for this can be understood by Fig. 13. We see that the distributions for Θ_1, Θ_2 , and Θ_3 are the same. So in the case of $\rho_2/\rho_1 \approx 1$ and $\rho_3/\rho_1 \approx 1$, there is a much larger number of lower values of Θ in the probability distribution constrained by these ratios of the SNRs. This

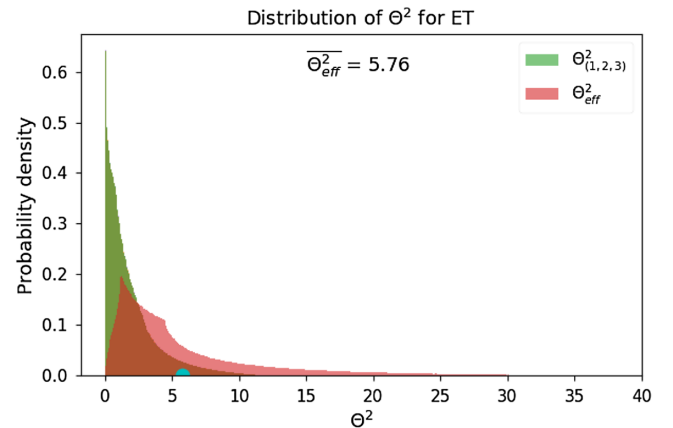


FIG. 13. The plot shows the probability distributions for Θ^2 for each of the three ET detectors and the probability distribution of Θ_{eff}^2 . The blue dot denotes the mean value $\overline{\Theta_{\text{eff}}^2}$.

results in smaller redshift and higher chirp mass in the respective distributions recovered for these parameters as explained above.

In order to see the variation in this bias due to the inclusion of segments of lower SNRs, we repeated the analysis for the following different detection criteria for 5-min segments.

- (i) *Criterion 1.*—A threshold value of accumulated effective SNR $\rho_{\text{eff}} > 8$ and the SNR for the i th segment in the j th detector $\rho_j^i > 3$ in at least one segment. This is the criteria which we have used in our main analysis in this paper.
- (ii) *Criterion 2.*—A threshold value of accumulated effective SNR $\rho_{\text{eff}} > 8$ and the SNR for the i th segment in the j th detector $\rho_j^i > 2$ in at least one segment.
- (iii) *Criterion 3.*—A threshold value of accumulated effective SNR $\rho_{\text{eff}} > 8$ and the SNR for the i th segment in the j th detector $\rho_j^i > 1$ in at least one segment.

The recovered median values vs the actual source values of chirp mass and redshift, using these three detection criteria, are shown in Fig. 15. The left panel shows the comparison for the chirp mass, and the right panel shows the comparison for the redshift. The top panel shows the comparison of the estimated median value with respect to

the actual value for criterion 1. When we repeat the analysis while including segments with $\rho_j^i > 2$, shown in the middle panel, we see that a few more sources cross the detection threshold and are shown in blue. The red points are the sources which were detectable with criterion 1, but their analysis now includes the additional low-SNR segments. The bottom row shows the subsequent inclusion of segments of $\rho_j^i > 1$, thus detecting a few more sources, shown in blue. While lowering the detection threshold detects a few more sources, there is also a slight worsening of the bias as we include segments of lower SNRs in the analysis. This can be clearly seen from the red points as we go from the top panel to the bottom panel. The underestimation of redshift and the overestimate of chirp are both slightly worsened.

Although the inclusion of segments of lower SNR worsens the bias, the error on the estimated parameters is lowered due to the additional information from these segments. The distribution of relative errors on chirp mass and redshift estimated using criterion 2 and criterion 3 are shown in Fig. 16. Comparing these with the error estimates obtained using criterion 1 shown in Fig. 9, we see that the additional segments contribute in reducing the relative errors, mainly for sources generating lower SNRs.

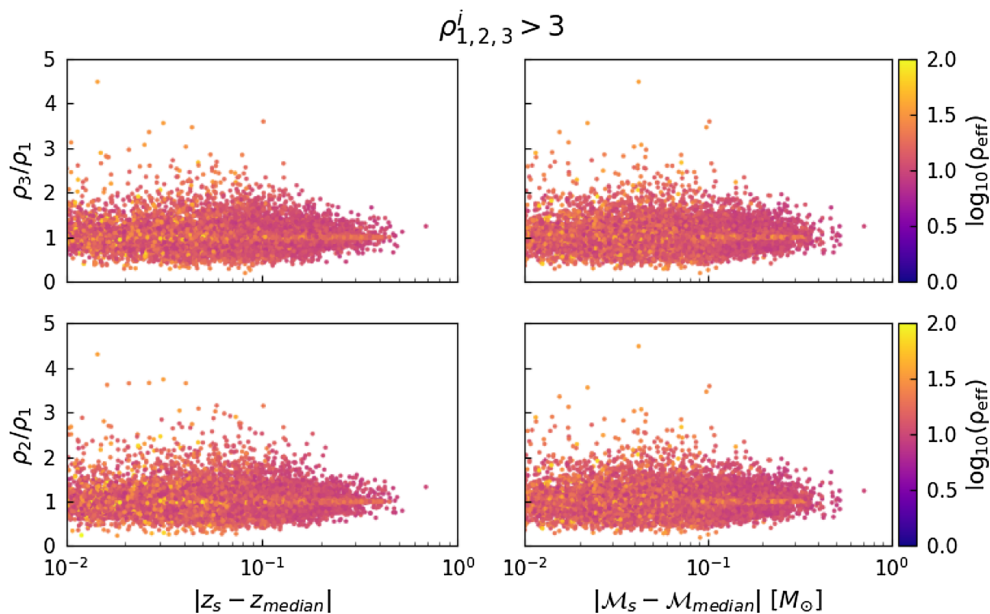


FIG. 14. The left panel shows the absolute value of bias in redshift as a function of ratios of SNRs, and the right panel shows the absolute value of bias in chirp mass as a function of ratios of SNRs.

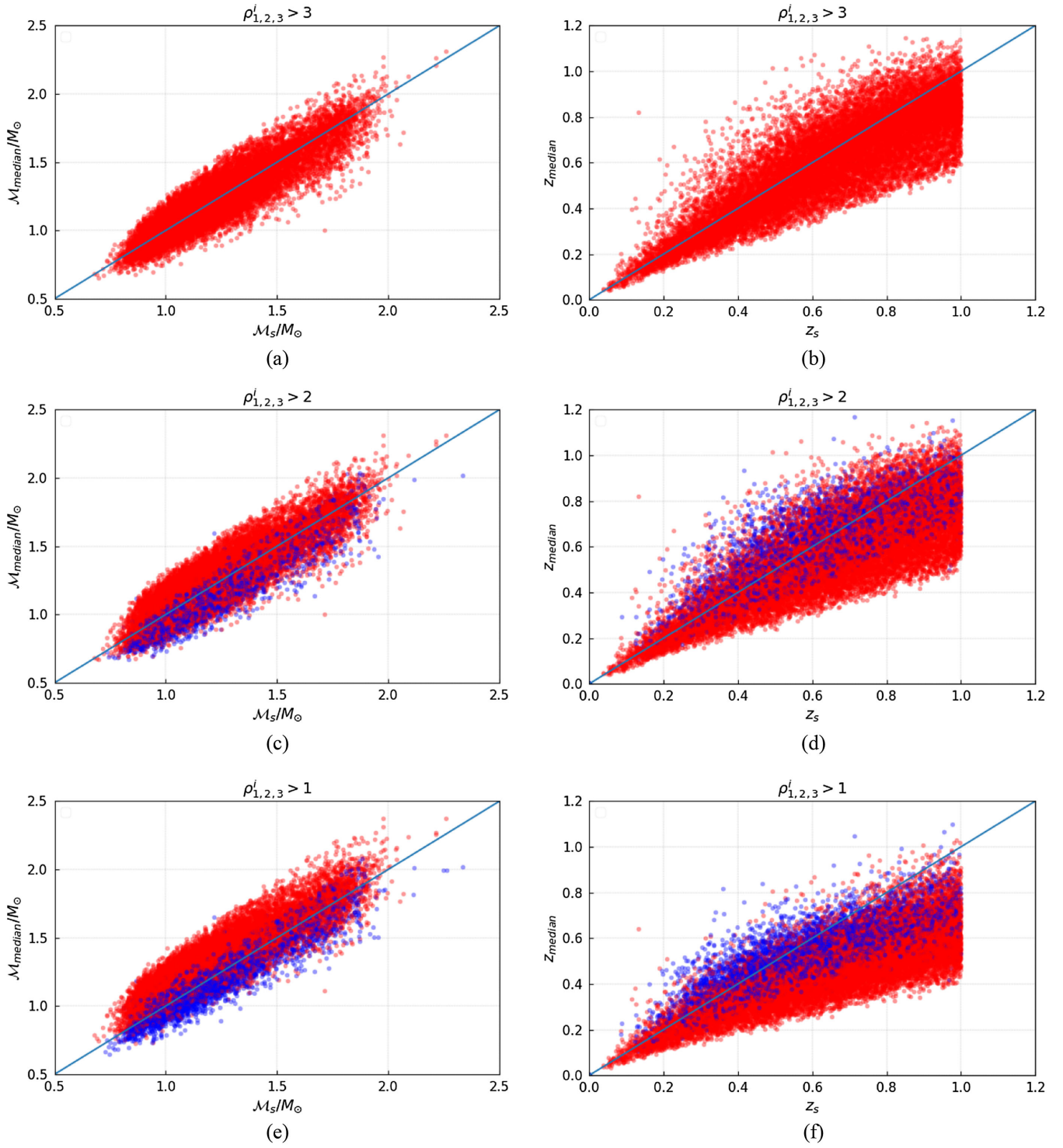


FIG. 15. The recovered median values vs the actual source values of the chirp mass \mathcal{M} (a,c,d) and redshift z (b,d,f). Top row: sources which are detectable using criterion 1. Middle row: The red point are the ones which were detectable with criterion 1 but were again detected and analyzed using criterion 2. The blue points are the ones which were not detectable using criterion 1 but are detectable using criterion 2. Bottom row: The red points are the ones which were detectable with criteria 1 but were again detected and analyzed using criterion 3. The blue points are the ones which were not detectable using criterion 1 but are detectable using criterion 3.

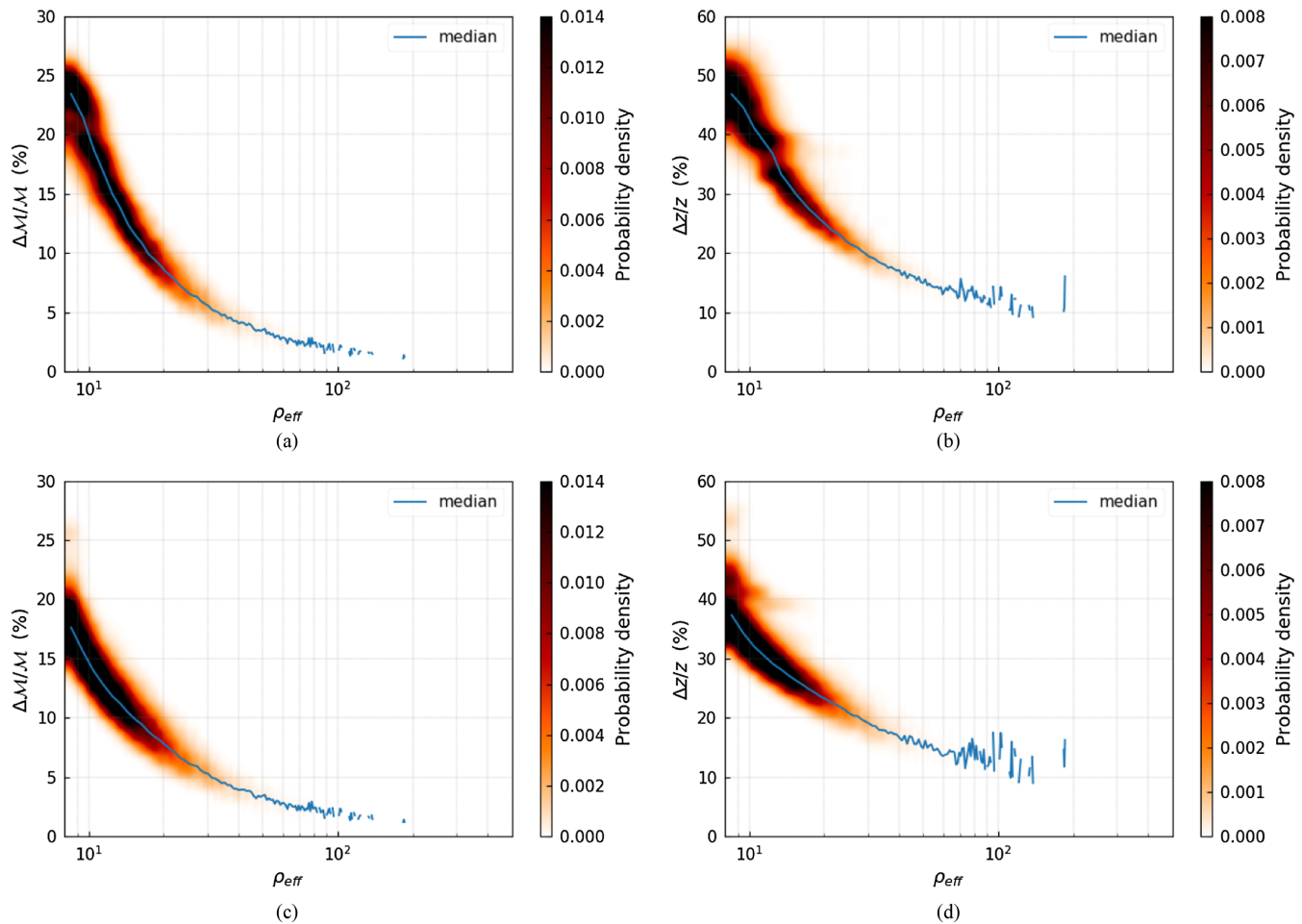


FIG. 16. Distribution of relative errors on chirp mass \mathcal{M} (left) and redshift z (right), estimated using criterion 2 (a,b) and criterion 3 (c,d).

-
- [1] B. P. Abbott, R. Abbott, T. D. Abbott, M. R. Abernathy, F. Acernese, K. Ackley, C. Adams, T. Adams, P. Addesso, R. X. Adhikari *et al.*, *Phys. Rev. Lett.* **116**, 061102 (2016).
- [2] R. Abbott, T. D. Abbott, S. Abraham, F. Acernese, K. Ackley, A. Adams, C. Adams, R. X. Adhikari, V. B. Adya, C. Affeldt *et al.*, *Phys. Rev. X* **11**, 021053 (2021).
- [3] B. P. Abbott, R. Abbott, T. D. Abbott, S. Abraham, F. Acernese, K. Ackley, C. Adams, R. X. Adhikari, V. B. Adya, C. Affeldt *et al.* (LIGO Scientific Collaboration and Virgo Collaboration), *Phys. Rev. X* **9**, 031040 (2019).
- [4] R. Abbott, T. D. Abbott, S. Abraham, F. Acernese, K. Ackley, C. Adams, R. X. Adhikari, V. B. Adya, C. Affeldt, M. Agathos *et al.* (LIGO Scientific Collaboration and Virgo Collaboration), *Phys. Rev. D* **102**, 043015 (2020).
- [5] R. Abbott, T. D. Abbott, S. Abraham, F. Acernese, K. Ackley, C. Adams, R. X. Adhikari, V. B. Adya, C. Affeldt, M. Agathos *et al.* (LIGO Scientific Collaboration and Virgo Collaboration), *Phys. Rev. Lett.* **125**, 101102 (2020).
- [6] B. P. Abbott, R. Abbott, T. D. Abbott, F. Acernese, K. Ackley, C. Adams, T. Adams, P. Addesso, R. X. Adhikari, V. B. Adya *et al.* (LIGO Scientific Collaboration and Virgo Collaboration), *Phys. Rev. Lett.* **119**, 161101 (2017).
- [7] A. Goldstein, P. Veres, E. Burns, M. S. Briggs, R. Hamburg, D. Kocevski, C. A. Wilson-Hodge, R. D. Preece, S. Poolakkil, O. J. Roberts *et al.*, *Astrophys. J. Lett.* **848**, L14 (2017).
- [8] V. Savchenko, C. Ferrigno, E. Kuulkers, A. Bazzano, E. Bozzo, S. Brandt, J. Chenevez, T. J. L. Courvoisier, R. Diehl, A. Domingo *et al.*, *Astrophys. J. Lett.* **848**, L15 (2017).
- [9] B. P. Abbott, R. Abbott, T. D. Abbott, F. Acernese, K. Ackley, C. Adams, T. Adams, P. Addesso, R. X. Adhikari, V. B. Adya *et al.*, *Astrophys. J. Lett.* **848**, L13 (2017).

- [10] D. A. Coulter, R. J. Foley, C. D. Kilpatrick, M. R. Drout, A. L. Piro, B. J. Shappee, M. R. Siebert, J. D. Simon, N. Ulloa, D. Kasen *et al.*, *Science* **358**, 1556 (2017).
- [11] E. Troja, L. Piro, H. van Eerten, R. T. Wollaeger, M. Im, O. D. Fox, N. R. Butler, S. B. Cenko, T. Sakamoto, C. L. Fryer *et al.*, *Nature (London)* **551**, 71 (2017).
- [12] G. Hallinan, A. Corsi, K. P. Mooley, K. Hotokezaka, E. Nakar, M. M. Kasliwal, D. L. Kaplan, D. A. Frail, S. T. Myers, T. Murphy *et al.*, *Science* **358**, 1579 (2017).
- [13] B. P. Abbott, R. Abbott, T. D. Abbott, F. Acernese, K. Ackley, C. Adams, T. Adams, P. Addesso, R. X. Adhikari, V. B. Adya *et al.*, *Astrophys. J. Lett.* **848**, L12 (2017).
- [14] S. Hild, M. Abernathy, F. Acernese, P. Amaro-Seoane, N. Andersson, K. Arun, F. Barone, B. Barr, M. Barsuglia, M. Beker *et al.*, *Classical Quantum Gravity* **28**, 094013 (2011).
- [15] M. Punturo, M. Abernathy, F. Acernese, B. Allen, N. Andersson, K. Arun, F. Barone, B. Barr, M. Barsuglia, M. Beker *et al.*, *Classical Quantum Gravity* **27**, 194002 (2010).
- [16] S. Dwyer, D. Sigg, S. W. Ballmer, L. Barsotti, N. Mavalvala, and M. Evans, *Phys. Rev. D* **91**, 082001 (2015).
- [17] B. P. Abbott, R. Abbott, T. D. Abbott, M. R. Abernathy, K. Ackley, C. Adams, P. Addesso, R. X. Adhikari, V. B. Adya, C. Affeldt *et al.*, *Classical Quantum Gravity* **34**, 044001 (2017).
- [18] D. Reitze, R. X. Adhikari, S. Ballmer, B. Barish, L. Barsotti, G. Billingsley, D. A. Brown, Y. Chen, D. Coyne, R. Eisenstein *et al.*, *Bull. Am. Astron. Soc.* **51**, 035 (2019).
- [19] S. Hild, S. Chelkowski, and A. Freise, [arXiv:0810.0604](https://arxiv.org/abs/0810.0604).
- [20] S. Hild, *Classical Quantum Gravity* **29**, 124006 (2012).
- [21] E. A. Huerta and J. R. Gair, *Phys. Rev. D* **83**, 044020 (2011).
- [22] E. A. Huerta and J. R. Gair, *Phys. Rev. D* **83**, 044021 (2011).
- [23] J. R. Gair, I. Mandel, M. C. Miller, and M. Volonteri, *Gen. Relativ. Gravit.* **43**, 485 (2011).
- [24] P. Amaro-Seoane and L. Santamaría, *Astrophys. J.* **722**, 1197 (2010).
- [25] B. S. Sathyaprakash *et al.*, [arXiv:1903.09260](https://arxiv.org/abs/1903.09260).
- [26] M. Maggiore, C. Van Den Broeck, N. Bartolo, E. Belgacem, D. Bertacca, M. A. Bizouard, M. Branchesi, S. Clesse, S. Foffa, J. García-Bellido *et al.*, *J. Cosmol. Astropart. Phys.* **03** (2020) 050.
- [27] T. Regimbau, T. Dent, W. Del Pozzo, S. Giampanis, T. G. F. Li, C. Robinson, C. Van Den Broeck, D. Meacher, C. Rodriguez, B. S. Sathyaprakash *et al.*, *Phys. Rev. D* **86**, 122001 (2012).
- [28] T. Regimbau, D. Meacher, and M. Coughlin, *Phys. Rev. D* **89**, 084046 (2014).
- [29] E. Belgacem, Y. Dirian, S. Foffa, E. J. Howell, M. Maggiore, and T. Regimbau, *J. Cosmol. Astropart. Phys.* **08** (2019) 015.
- [30] W. Zhao and L. Wen, *Phys. Rev. D* **97**, 064031 (2018).
- [31] M. L. Chan, C. Messenger, I. S. Heng, and M. Hendry, *Phys. Rev. D* **97**, 123014 (2018).
- [32] N. Singh and T. Bulik, *Phys. Rev. D* **104**, 043014 (2021).
- [33] T. Bulik, K. Belczyński, and B. Rudak, *Astron. Astrophys.* **415**, 407 (2004).
- [34] P. Jaranowski, A. Królak, and B. F. Schutz, *Phys. Rev. D* **58**, 063001 (1998).
- [35] T. Accadia, F. Acernese, M. Alshourbagy, P. Amico, F. Antonucci, S. Aoudia, N. Arnaud, C. Arnault, K. G. Arun, P. Astone *et al.*, *J. Instrum.* **7**, P03012 (2012).
- [36] F. Acernese, M. Agathos, K. Agatsuma, D. Aisa, N. Allemandou, A. Allocca, J. Amarni, P. Astone, G. Balestri, G. Ballardín *et al.*, *Classical Quantum Gravity* **32**, 024001 (2015).
- [37] B. Allen, W. G. Anderson, P. R. Brady, D. A. Brown, and J. D. E. Creighton, *Phys. Rev. D* **85**, 122006 (2012).
- [38] B. S. Sathyaprakash and S. V. Dhurandhar, *Phys. Rev. D* **44**, 3819 (1991).
- [39] S. R. Taylor and J. R. Gair, *Phys. Rev. D* **86**, 023502 (2012).
- [40] R. O’Shaughnessy, V. Kalogera, and K. Belczynski, *Astrophys. J.* **716**, 615 (2010).
- [41] L. S. Finn, *Phys. Rev. D* **53**, 2878 (1996).
- [42] M. Maggiore, *Gravitational Waves. Vol. 1: Theory and Experiments*, Oxford Master Series in Physics (Oxford University Press, New York, 2007), ISBN 978-0-19-857074-5, 978-0-19-852074-0.
- [43] R. Abbott, T. D. Abbott, F. Acernese, K. Ackley, C. Adams, N. Adhikari, R. X. Adhikari *et al.* (The LIGO Scientific Collaboration, the Virgo Collaboration, and the KAGRA Collaboration), [arXiv:2111.03606](https://arxiv.org/abs/2111.03606).
- [44] É. Aubourg, S. Bailey, J. E. Bautista, F. Beutler, V. Bhardwaj, D. Bizyaev, M. Blanton, M. Blomqvist, A. S. Bolton, J. Bovy *et al.*, *Phys. Rev. D* **92**, 123516 (2015).
- [45] M. Adachi and M. Kasai, *Prog. Theor. Phys.* **127**, 145 (2012).
- [46] N. Singh, T. Bulik, K. Belczynski, and A. Askar, *Astron. Astrophys.* **667**, A2 (2022).
- [47] <http://www.et-gw.eu/index.php/etsensitivities>.
- [48] J. M. Lattimer, *Annu. Rev. Nucl. Part. Sci.* **62**, 485 (2012).
- [49] <https://jantoniadis.wordpress.com/research/ns-masses/>.